JGR Atmospheres

RESEARCH ARTICLE
10.1029/2025JD043695

An Unusual Winter Ozone Event in Colorado

Andrew O. Langford[1], Kenneth C. Aikin[1,2], Raul J. Alvarez II[1], Sunil Baidar[1,2], W. Alan Brewer[1], Steven S. Brown[1], Matthew M. Coggon[1,2], Patrick D. Cullis[2,3], Jessica B. Gilman[1], Georgios I. Gkatzelis[1,2,4], Detlev Helmig[5], Bryan J. Johnson[3], K. Emma Knowland[6,7], Rajesh Kumar[8], Aaron D. Lamplugh[1,2,9], Brandi J. McCarty[1,2], Ann M. Middlebrook[1], Gabriele Pfister[10], Jeff Peischl[1,2,3], Irina Petropavlovskikh[2,3], Pamela S. Rickly[1,2,9], Michael A. Robinson[1,2], Andrew W. Rollins[1], Scott P. Sandberg[1], Christoph J. Senff[1,2], and Carsten Warneke[1]

[1]NOAA Chemical Sciences Laboratory, Boulder, CO, USA, [2]Cooperative Institute for Research in Environmental Sciences, University of Colorado, Boulder, CO, USA, [3]NOAA Global Monitoring Laboratory, Boulder, CO, USA, [4]Now at Institute of Energy and Climate Research, IEK-8: Troposphere, Forschungszentrum Jülich GmbH, Jülich, Germany, [5]Boulder Air LLC, Boulder, CO, USA, [6]Morgan State University, GESTAR-II, Baltimore, MD, USA, [7]NASA Goddard Space Flight Center, Global Modeling and Assimilation Office, Greenbelt, MD, USA, [8]NSF NCAR Research Applications Laboratory, Boulder, CO, USA, [9]Now at Air Pollution Control Division, Colorado Department of Public Health and Environment, Denver, CO, USA, [10]NSF NCAR Atmospheric Chemistry Observations and Modeling Laboratory, Boulder, CO, USA

Abstract Surface ozone (O_3) mixing ratios exceeding the National Ambient Air Quality Standard were measured at rural monitors along the Colorado Front Range on 17 April 2020 during the COVID-19 lockdown. This unusual episode followed back-to-back upslope snowstorms and coincided with the presence of a deep stratospheric intrusion, but ground-based lidar and ozonesonde measurements show that little, if any, of the O_3-rich lower stratospheric air reached the surface. Instead, the statically stable lower stratospheric air suppressed the growth of the daytime boundary layer and trapped nitrogen oxides ($NO_x = NO + NO_2$) and volatile organic compounds (VOCs) emitted by motor vehicles and oil and natural gas (O&NG) operations near the ground where the clear skies and extensive snow cover triggered a short-lived photochemical episode similar to those observed in the O&NG producing basins of northeastern Utah and southwestern Wyoming. In this study, we use a combination of lidar, ozonesonde, and surface measurements, together with the WRF-Chem and Goddard Earth Observing System composition forecast models, to describe the stratospheric intrusion and characterize the boundary layer structure, HYSPLIT back trajectories to show the low-level transport of O_3 and its precursors to the exceedance sites, and surface measurements of NO_x and VOCs together with a 0-D box model to investigate the roles of urban and O&NG emissions and the COVID-19 quarantine in the O_3 production. The box model showed the O_3 production to be NO_x saturated, such that the NO_x reductions associated with COVID-19 exacerbated the event rather than mitigating it.

Plain Language Summary A growing body of research has shown that high ground-level ozone (O_3) can adversely affect both human health and welfare. High O_3 concentrations are usually associated with urban areas and hot summer days, but under certain conditions they can also occur in rural areas at very cold temperatures. These winter ozone events have been seen in the remote oil and natural gas (O&NG) producing basins of northeastern Utah and southwestern Wyoming when nitrogen oxides and volatile organic compounds emitted by O&NG activities are trapped near the surface by extremely shallow inversions. These inversions are caused by very cold temperatures with snow-cover an essential ingredient that both increases the atmospheric stability and drives the photochemistry by reflecting sunlight off the surface. These winter ozone events have previously been observed only in the sparsely populated O&NG basins to the west, but here we describe a similar event that occurred in the more densely populated Front Range of Colorado during the COVID-19 quarantine.

Key Points:

- Ozone concentrations exceeding the National Ambient Air Quality Standard were measured along the Colorado Front range following a major snowstorm
- Photochemical precursors from regional sources were trapped near the surface by an unusually shallow daytime boundary layer
- The shallow boundary layer was caused in part by descent of stable stratospheric air into the lower troposphere

Supporting Information:

Supporting Information may be found in the online version of this article.

Correspondence to:

A. O. Langford,
andrew.o.langford@noaa.gov

Citation:

Langford, A. O., Aikin, K. C., Alvarez, R. J., II, Baidar, S., Brewer, W. A., Brown, S. S., et al. (2025). An unusual winter ozone event in Colorado. *Journal of Geophysical Research: Atmospheres*, *130*, e2025JD043695. https://doi.org/10.1029/2025JD043695

Received 21 FEB 2025
Accepted 13 JUL 2025

Author Contributions:

Conceptualization: Andrew O. Langford
Data curation: Andrew O. Langford, Kenneth C. Aikin, Raul J. Alvarez II, Sunil Baidar, W. Alan Brewer, Matthew M. Coggon, Patrick D. Cullis, Jessica B. Gilman, Georgios I. Gkatzelis, Detlev Helmig, Bryan J. Johnson, Aaron D. Lamplugh, Brandi J. McCarty, Jeff Peischl, Irina Petropavlovskikh, Pamela S. Rickly, Michael A. Robinson,

1. Introduction

Ground-level ozone (O_3) is one of the six "criteria" pollutants deemed particularly harmful to human health and welfare and made subject to National Ambient Air Quality Standards (NAAQS) by the US Clean Air Act (Karstadt et al., 1993). Unlike the other gaseous criteria pollutants (i.e., NO_2, SO_2, and CO), O_3 is not directly emitted by anthropogenic activities, but is a secondary pollutant formed by photochemical reactions of nitrogen

Andrew W. Rollins, Scott P. Sandberg, Christoph J. Senff, Carsten Warneke
Formal analysis: Andrew O. Langford
Funding acquisition: Andrew O. Langford
Investigation: Andrew O. Langford, Raul J. Alvarez II, Sunil Baidar, W. Alan Brewer, Matthew M. Coggon, Patrick D. Cullis, Jessica B. Gilman, Georgios I. Gkatzelis, Detlev Helmig, Bryan J. Johnson, Rajesh Kumar, Aaron D. Lamplugh, Brandi J. McCarty, Ann M. Middlebrook, Gabriele Pfister, Jeff Peischl, Irina Petropavlovskikh, Pamela S. Rickly, Michael A. Robinson, Andrew W. Rollins, Scott P. Sandberg, Christoph J. Senff, Carsten Warneke
Methodology: Andrew O. Langford
Project administration: Andrew O. Langford
Resources: Andrew O. Langford, K. Emma Knowland
Software: Andrew O. Langford, Kenneth C. Aikin, Sunil Baidar, Matthew M. Coggon, Rajesh Kumar
Supervision: Andrew O. Langford, Steven S. Brown
Validation: Andrew O. Langford
Visualization: Andrew O. Langford, Sunil Baidar, Matthew M. Coggon, K. Emma Knowland, Gabriele Pfister
Writing – original draft: Andrew O. Langford
Writing – review & editing: Andrew O. Langford, Steven S. Brown, Matthew M. Coggon, K. Emma Knowland, Jeff Peischl, Christoph J. Senff

oxides ($NO_x = NO + NO_2$) and volatile organic compounds (VOCs) originating from natural or anthropogenic sources (Jaffe et al., 2018). Surface O_3 mixing ratios usually peak in summer when photochemical production is accelerated by warm temperatures and high solar fluxes (Sillman & Samson, 1995) and most exceedances of the NAAQS, currently set at 70 parts-per-billion by volume (ppbv) for the maximum daily 8-hr average (MDA8), occur in or around urban areas during the so-called "ozone season" from May to September.

A striking exception to this paradigm was first described by Schnell et al. (2009) who documented multi-day wintertime episodes with hourly O_3 mixing ratios in excess of 150 ppbv in the rural Upper Green River Basin of Wyoming (Carter & Seinfeld, 2012; Rappenglück et al., 2014). Similar high-O_3 episodes were subsequently observed in the nearby Uinta Basin of northeastern Utah (Martin et al., 2011) and three Uintah Basin Winter Ozone Study field campaigns (Ahmadov et al., 2015; Edwards et al., 2014; Edwards et al., 2013; Helmig et al., 2014) were conducted in 2012–2014 to investigate this phenomenon. These campaigns and related studies determined that the high O_3 episodes occurred when NO_x and VOCs emitted by local oil and natural gas (O&NG) operations built up within the unusually shallow boundary layers that form above the basin-like terrain of these remote O&NG fields at very cold temperatures (Lareau et al., 2013; Lyman & Tran, 2015; McCaffrey et al., 2019; Neemann et al., 2015; Oltmans et al., 2014; Schnell et al., 2016). Snow cover proved to be an essential component of these episodes that: (a) enhanced the actinic flux by increasing the surface albedo, and (b) reinforced the boundary layer stability by decreasing the sensible heat flux (Bader & McKee, 1985).

Persistent cold pools form in other O&NG fields with basin-like topography (Mansfield & Hall, 2018), but are much less likely to occur in those with more open terrain such as the Wattenberg Gas Field (WGF) in the Denver-Julesburg Basin of northeastern Colorado. The WGF, which encroaches on the northern Front Range urban corridor, lies within the Denver Metro/Northern Front Range (DM/NFR) O_3 non-attainment area, which was recently downgraded from "serious" to "severe 15" non-attainment of the 2008 O_3 NAAQS of 75 ppbv. Numerous studies (e.g. (Cheadle et al., 2017; Flocke et al., 2020; Helmig, 2020; McDuffie et al., 2016; Pétron et al., 2012; Pétron et al., 2014)) have investigated the impact of O&NG emissions on O_3 mixing ratios in the DM/NFR, but there have been no reported instances of winter O_3 episodes such as those seen in the Uinta and Green River Basins. Here, we describe such an event that resulted in the only NAAQS exceedances in the US on 17 April 2020 (Figure 1).

In this short-lived episode, which occurred early in the COVID-19 lockdown (He et al., 2023), the shallow inversion was reinforced by the descent of statically stable lower stratospheric air deep into the lower troposphere. In this study, we use a combination of lidar, ozonesonde, and surface measurements, together with the WRF-Chem and Goddard Earth Observing System composition forecast (GEOS-CF) models, to describe the stratospheric intrusion and characterize the boundary layer structure, surface measurements of NO_x and VOCs together with a 0-D box model (Rickly et al., 2023) to evaluate the production of O_3 by local photochemistry, and HYSPLIT back trajectories (Stein et al., 2015), together with VOC ratios, to assess the contributions of mobile sources and O&NG operations to the episode.

2. Meteorological Context

Back-to-back upslope storms associated with a slow-moving upper-level low brought heavy snow and record low temperatures to the DM/NFR between April 11 and 16, 2020. The first cold front arrived on the night of April 11 and the temperature in the Boulder-Longmont area decreased from 15°C to −5°C in less than 6 hr (Figure 2a) with snow beginning in the early morning hours of April 12 as the winds shifted to the north (Figure 2b). The snowfall was heaviest in and along the foothills west of Boulder where moist air from the Gulf of Mexico orographically lifted by the higher terrain collided with cold air from the north and west. Snow continued to fall through the next 48 hr with more than 42 cm (16.5 in) accumulating at the NOAA David Skaggs Research Center (DSRC) in southwest Boulder (Figure 3). Relatively little snow fell in the O&NG fields to the east, however, with only 3 cm of snow measured at the Denver International Airport (DIA) National Weather Service office. The DIA station did measure a record low daily high temperature of −3.9°C on the afternoon of April 13, however, and the radiative cooling that occurred after the skies cleared later that night resulted in a record low temperature of −9.4°C on the morning of April 14 (Figure 2b). The temperature climbed to 8°C by the afternoon, however, and the skies remained clear except for a few scattered clouds above the foothills.

The spring-like conditions were short lived, however, as the second storm arrived on the 15th and brought an additional 43 cm (16.9 in) of snow to the DSRC and another 61 cm (24 in) to the nearby foothills. This storm

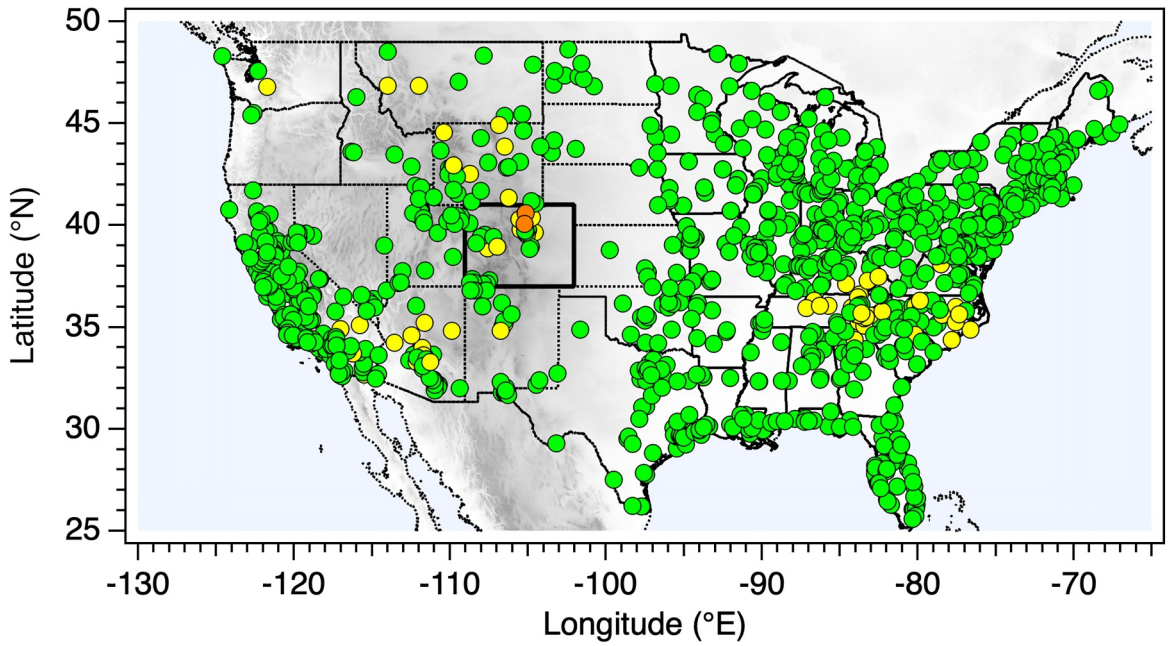

Figure 1. MDA8 O_3 measured by the roughly 1,200 regulatory monitors that reported to the US EPA on 17 April 2020. Colorado is outlined in heavy black. The symbols are colored according to the EPA Air Quality Index with green representing "good" (0–54 ppbv), yellow "moderate" (55–70 ppbv), orange "unhealthy for sensitive groups" (71–85 ppbv). The Boulder Reservoir (BOUR, 77 ppbv) and Ft. Collins-West (FTCW, 75 ppbv) monitors measured the highest MDA8 O_3 in the US on that day.

broke the seasonal snowfall record for Boulder which had stood since the winter of 1908–1909. This storm also brought significantly more snow to the eastern plains with 10 cm (4 in.) measured at DIA. The skies cleared around midnight and the subsequent radiative cooling contributed to another record low of −11.7°C at the DIA on the morning of the 17th. As on the 14th, the skies remained clear throughout the day with the temperature peaking at 8°C in the afternoon.

3. Surface Ozone

The similar temperatures and solar irradiance on the 14th and 17th suggest a similar potential for photochemical production, but Figure 3 indicates that the measured O_3 mixing ratios on these two days were very different. Figures 3a and 3b show the MDA8 O_3 mixing ratios measured by all of the regulatory and non-regulatory monitors operated by private, state, and federal agencies (see Supporting Information S1) on April 14 and 17 respectively, superimposed on the corresponding (cloud-free) Terra-MODIS images, which show more extensive snow cover across the WGF on the 17th. The filled circles represent the regulatory monitors from Figure 1 and include the Boulder Reservoir (BOUR) and Ft. Collins-West (FTCW) monitors that exceeded the NAAQS with MDA8 mixing ratios of 77 and 75 ppbv, respectively on the 17th. The filled squares show non-regulatory research monitors operated by NOAA GML at Niwot Ridge (NWR) and Table Mountain (BOS), and by NOAA CSL at the DSRC in Boulder. The filled diamonds show the non-regulatory monitors operated by Boulder A.I.R. at the Longmont Municipal Airport (LMA) and Longmont Union Reservoir (LUR). The measurements from these sites are described in more detail in the Supporting Information S1. Figure 3a shows that all of the monitors in the DM/NFR measured "good" MDA8 O_3 mixing ratios on the 14th, but Figure 3b shows that most measured mixing ratios considered "moderate" or even "unhealthy for sensitive groups" on the 17th. The highest MDA8 O_3 concentrations (orange symbols) were measured in the largely rural area bounded by the WGF and the foothills between Boulder and Ft. Collins; the lowest (green symbols) were measured in the more densely populated Denver urban area.

Figure 4a displays time series of the hourly O_3 measurements from all of the monitors shown in Figure 3. The measurements from the high elevation (>2.5 km above mean sea level, a.s.l.) "baseline" monitors at Blackhawk (BHWK), NWR, and Rocky Mountain National Park are plotted in black with the measurements from the BOUR and BOS monitors plotted in red. The measurements from the La Casa NCORE site (CASA) are plotted in blue

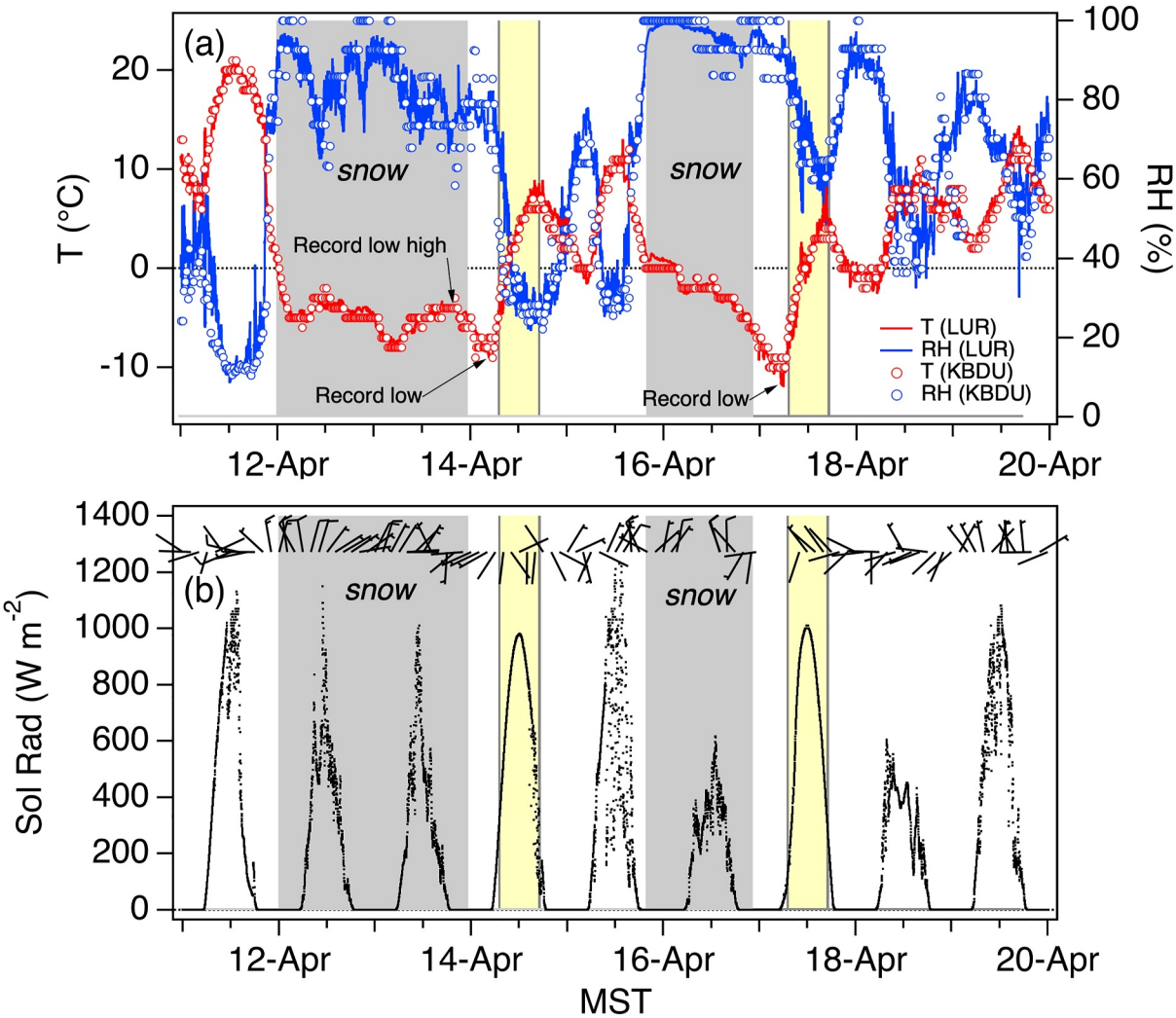

Figure 2. (a) Temperature and relative humidity from the Longmont Union Reservoir (LUR) and Boulder Municipal Airport (KBDU) stations. (b) Solar irradiance and wind measurements from LUR. Snow periods are highlighted in gray and the photochemically active periods on the 14th and 17th in yellow.

and the remaining time series are plotted in gray. The highest 1-hr O_3 (83 ppbv) was recorded by the BOUR monitor at 1700 MST on April 17. The heavy snowfall the previous night took this station offline for most of the morning and the early afternoon so we fill in this gap with the measurements from the NOAA GML monitor (BOS) located about 6 km to the north at the Department of Commerce field site on Table Mountain. The BOS monitor recorded a very similar peak 1-hr value (82 ppbv) as the BOUR monitor and the same MDA8 O_3 (77 ppbv). Peak 1-hr O_3 mixing ratios greater than 70 ppbv were also measured by the FTCW, LMA, LUR, and DSRC monitors (cf. Figure 3b). The lowest 1-hr O_3 (0 ppbv) measured on April 17 was recorded at 0300 MST by the La Casa NCORE site (CASA, 1.60 km a.s.l.). This monitor is located ≈33 km southeast of the DSRC and near the confluence of I-25 and I-70 in Denver. This urban monitor also measured much lower MDA8 O_3 (43 ppbv) than the rural sites to the north with comparable values reported by all of the other monitors in Denver.

Figure 3b shows that the three baseline monitors are almost equally spaced (about 25 km) along a roughly north-to-south line in the mountains to the west of the NFR, and the measurements from these 3 sites appear very similar (the BHWK monitor was offline on April 14), suggesting that the measurements were usually representative of the lower free troposphere. Figure 4b is similar to Figure 4a, but plots only the mean of the measurements from the three baseline monitors in black (±5 ppbv in dark gray) and the BOUR (red), BOS (dotted red) and CASA (blue) time series. The BOUR monitor is located adjacent to the primary highway connecting Boulder and Longmont and the early morning measurements in Figure 4 show clear signs of NO_x titration, but the BOS monitor is located

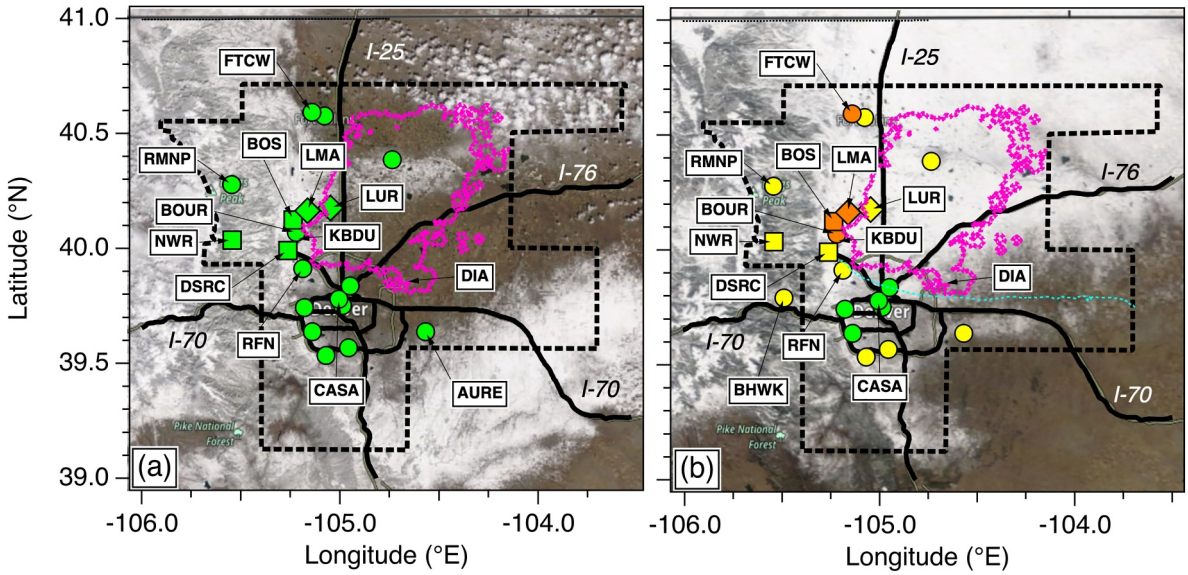

Figure 3. MDA8 O_3 mixing ratios (Air Quality Index) on (a) April 14 and (b) 17 April 2020, superimposed on the daily (10:30 local time) corrected reflectance (True Color) Terra/MODIS images from NASA/Worldview (https://worldview.earthdata.nasa.gov/, last accessed 19 February 2025). The black-dashed lines show the DM/NFR O_3 non-attainment area and the dotted magenta lines the Wattenberg Gas Field. The dotted cyan line in (b) shows the path of the GML ozonesonde (Section 4.2).

on a more isolated grass-covered mesa (1.69 km a.s.l.) and these measurements appear very similar to those from the baseline monitors between the 11th and 16th, indicating that there was little photochemical production of O_3 or deposition to the snow-covered surface (Helmig et al., 2007).

The BOS monitor measured nearly 20 ppbv more O_3 than the baseline monitors on the afternoon of the 17th, and 10–15 ppbv more O_3 on the 18th. The CASA measurements appear very different, however, and were 5–10 ppbv lower than the baseline mixing ratios during the day and as much as 50 ppbv lower during the late night and early morning. This shows net destruction of O_3 in this high traffic area, and the effects of NO_x titration are particularly striking in the measurements from the morning of the 17th when all of the surface O_3 was titrated between 0300 and 0500 MST. The dashed blue line shows that the total O_x mixing ratios (i.e., NO_2 + O_3) at CASA were accordingly similar to the baseline O_3 between the 11th and 16th. The O_x was higher than the baseline O_3 on the 17th and 18th, yet nearly 10 ppbv smaller than the average O_3 measured by the rural BOS monitor to the northwest the following night.

4. Stratospheric Influence

4.1. Upper Air Analyses

It is well established that deep stratospheric intrusions can increase surface O_3 and even cause exceedances of the NAAQS in the NFR (Langford et al., 2009) and the upper-level low responsible for the late season snowstorms also spawned several intrusions as it crossed North America. The 0000 UT 300 hPa (≈9.2 km a.s.l.) potential vorticity (PV) distributions, a tracer for lower stratospheric air, from the NASA MERRA-2 Reanalysis (Gelaro et al., 2017; Knowland et al., 2017) displayed on the left side of Figure 5 show the progression of two of these intrusions across the southern US. The corresponding 500 hPa O_3 distributions from the NASA GEOS-CF model (Keller et al., 2021; Knowland et al., 2017; Knowland et al., 2022) (middle) and 5 km a.s.l. (≈540 hPa) O_3 distributions from the NCAR Weather Research Forecasting with Chemistry (WRF-Chem) (Kumar et al., 2021) model (right) show their impacts on mid-tropospheric O_3.

Figure 5a shows an elongated trough trailing behind the main low-pressure center over eastern Canada and curving cyclonically across Colorado and the Southwestern US on the afternoon of April 14. The band of elevated PV along the leading edge of the trough near the southeast corner of Colorado shows the tropopause fold, but Figures 5b and 5c show that the equatorward sloping tongue of high O_3 passed well to the south of Colorado. The intrusion moved eastward and over the Atlantic Ocean over the next couple of days as a second trough dropped

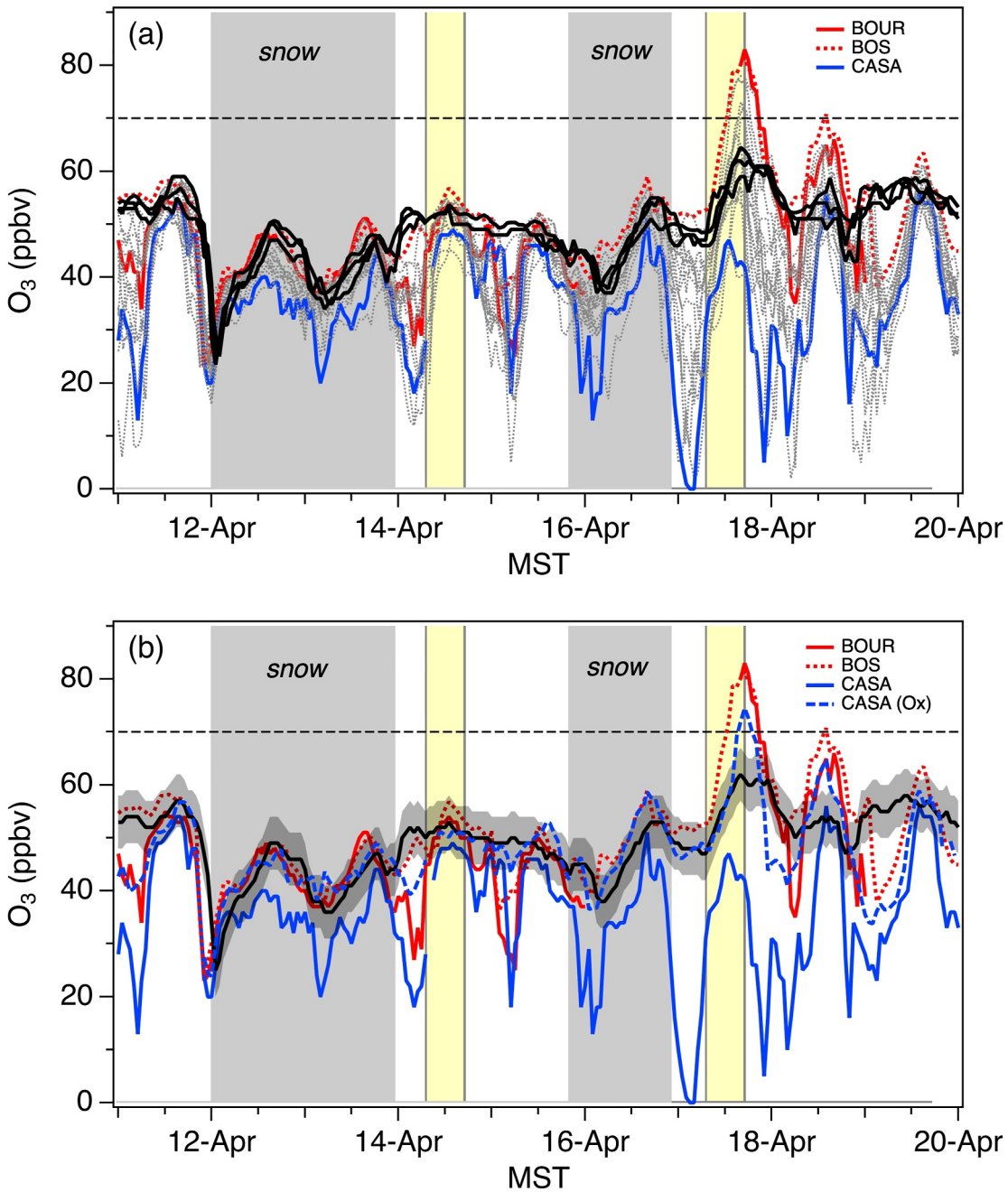

Figure 4. (a) Time series of the hourly O_3 measurements from all of the monitors shown in Figure 3. The measurements from the high elevation baseline sites (BHWK, Niwot Ridge, and Rocky Mountain National Park) are plotted in black. The measurements from the Boulder Reservoir (BOUR) and BOS monitors which measured the highest hourly O_3 on April 17 are plotted in red and the measurements from the CASA monitor which measured the lowest hourly O_3 are plotted in blue. (b) Same as (a), but showing only the measurements from the BOUR, BOS, and CASA monitors together with the mean baseline mixing ratios (black, ±5 ppbv in dark gray). The dashed blue line shows the CASA O_x (NO_2 + O_3) mixing ratios and the horizontal dashed lines the 2015 National Ambient Air Quality Standard.

down from Canada (Figures 5d–5f) and developed a tropopause fold above the Pacific Northwest. This intrusion evolved into an elongated streamer as it moved into Colorado behind the snowstorm and the analyses for the afternoon of April 17 in Figure 5j shows the narrow filament of high PV air stretching across southern Wyoming and northeastern Colorado and the WRF-Chem analysis (Figures 5k and 5l) show the narrow filament of high O_3 directly above Colorado.

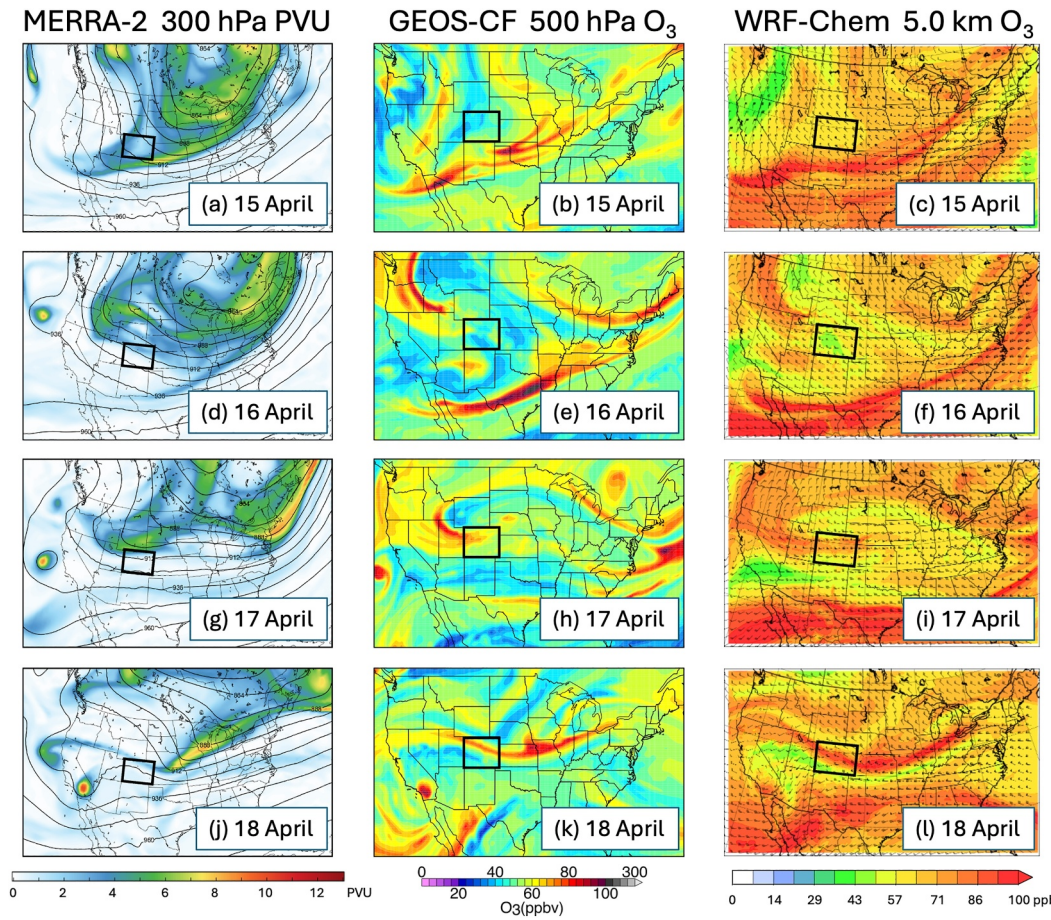

Figure 5. NASA MERRA-2 300 hPa potential vorticity distributions (left), NASA Goddard Earth Observing System composition forecast 500 hPa O_3 distributions (middle), and NCAR WRF-Chem 5 km a.s.l. O_3 distributions (right) at, from top to bottom, 0000 UT on April 15, 16, 17, and 18 (1700 MST on April 14, 15, 16, and 17). Colorado is outlined in black. The MERRA-2 images were downloaded from the publicly accessible archives at https://fluid.nccs.nasa.gov/reanalysis/classic_merra2/ (last access 19 February 2025). The WRF-Chem images were downloaded from the publicly accessible archive at https://www.acom.ucar.edu/firex-aq/forecast.shtml (last access 19 February 2025).

Figure 6 displays vertical cross-sections of the O_3 distributions from the NASA GEOS-CF model (Keller et al., 2021; Knowland et al., 2022) along latitudinal and longitudinal transects through Boulder (vertical dashed lines) on the afternoons of April 14 and 17. Figures 6a and 6b show the downward sloping tongue of lower stratospheric air from the first intrusion far descending isentropically well to the south of Boulder in agreement with Figures 5a, 5b and 6c shows the second intrusion poised directly above Colorado in agreement with Figures 5g and 5h. Figures 6c and 6d show this deep intrusion increasing the surface mixing ratios to 50–60 ppbv along the foothills near Boulder and to 60–65 ppbv in the mountains to the south, in agreement with the measurements from the high elevation baseline monitors (cf. Figure 4b).

4.2. Upper Air Measurements

The GEOS-CF analyses can also be compared to the O_3 vertical distributions measured by the ground-based TOPAZ lidar at the DSRC (Alvarez et al., 2011; Langford et al., 2019). TOPAZ, which is part of the NASA-supported Tropospheric Ozone Lidar Network (TOLNet) (Newchurch et al., 2016), measures O_3 and 0.294 μm aerosol backscatter (ß) profiles from about 20 m above ground level (a.g.l.) to roughly 8 km a.g.l. (depending on the total extinction and solar background) with a time resolution of 10 min and with an effective O_3 vertical resolution ranging from roughly 10 m near the surface to about 900 m at the far end of the measurement range. The total uncertainty of the O_3 measurements increases from approximately 3 ppbv below 4 km a.g.l. To about 10 ppbv at 8 km a.g.l. NOAA CSL also operated a commercial Doppler lidar that measured aerosol

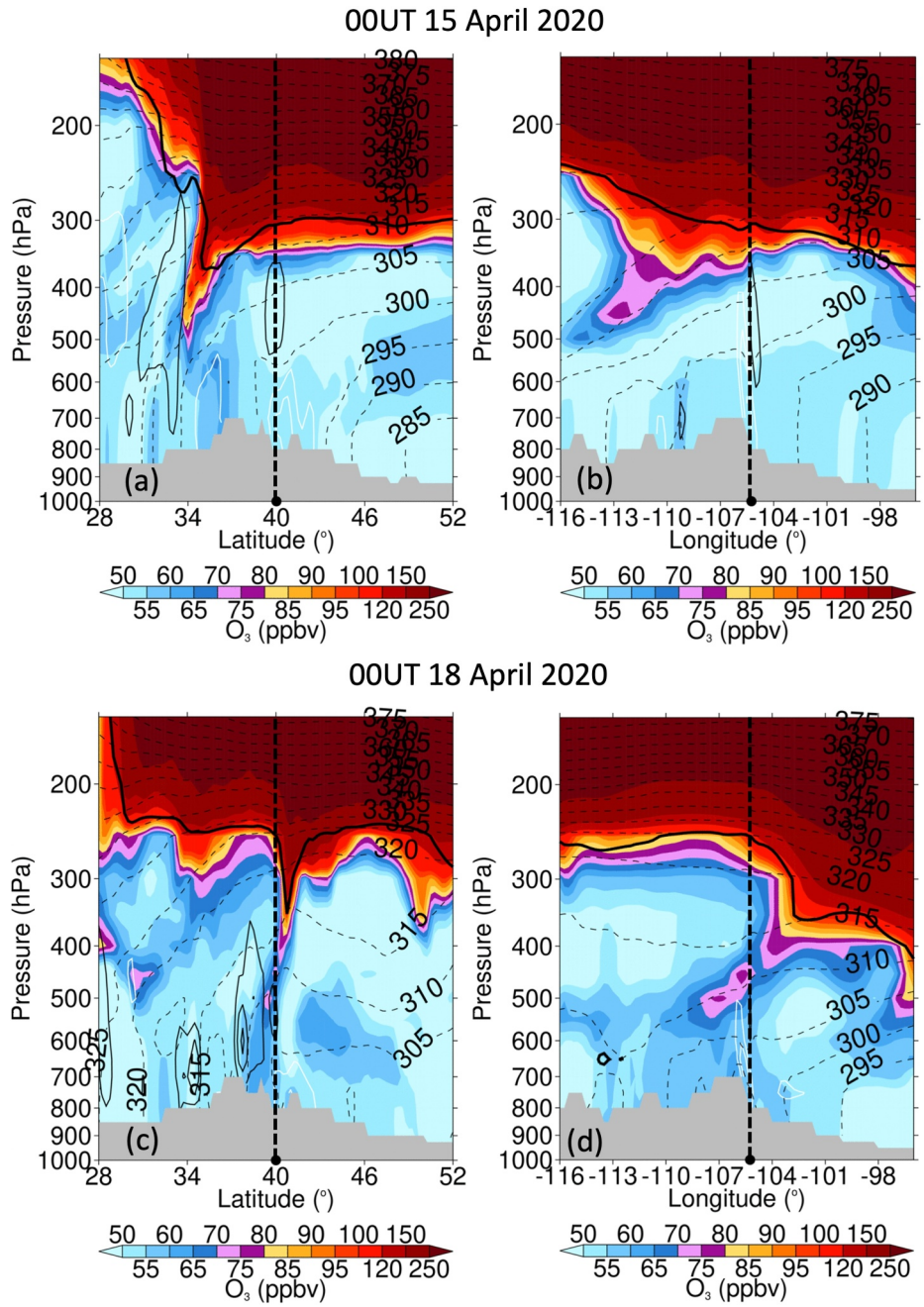

Figure 6. Vertical cross-sections of the O_3 mixing ratios (color) along latitudinal (left) and longitudinal (right) transects passing through Boulder (vertical dashed lines) at 0000 UT on April 15 (top) and 18 April 2020 (bottom) from the NASA Goddard Earth Observing System composition forecast model. Equivalent potential temperature (dashed contour lines, 5 K intervals) and the dynamical tropopause isosurface of 2 potential vorticity units (PVU: 10^{-6} K m^2 kg^{-1} s^{-1}; thick black contour), vertical velocity (solid contour lines, 10 hPa hr^{-1} intervals, with white contours for descent and black contours for ascent) are drawn. The terrain is indicated in gray.

backscatter in the near-infrared (1.54 μm), horizontal windspeed and direction, and vertical velocity variance from the roof of the DSRC.

Figure 7 displays time-height curtain plots of the O_3 (top) and backscatter (bottom) distributions measured by TOPAZ on April 14 (left) and April 17 (right). The colored horizontal stripes in the upper panels show the in situ measurements from the monitor located in the TOPAZ truck, which sampled air at 5 m a.g.l., and the NWR

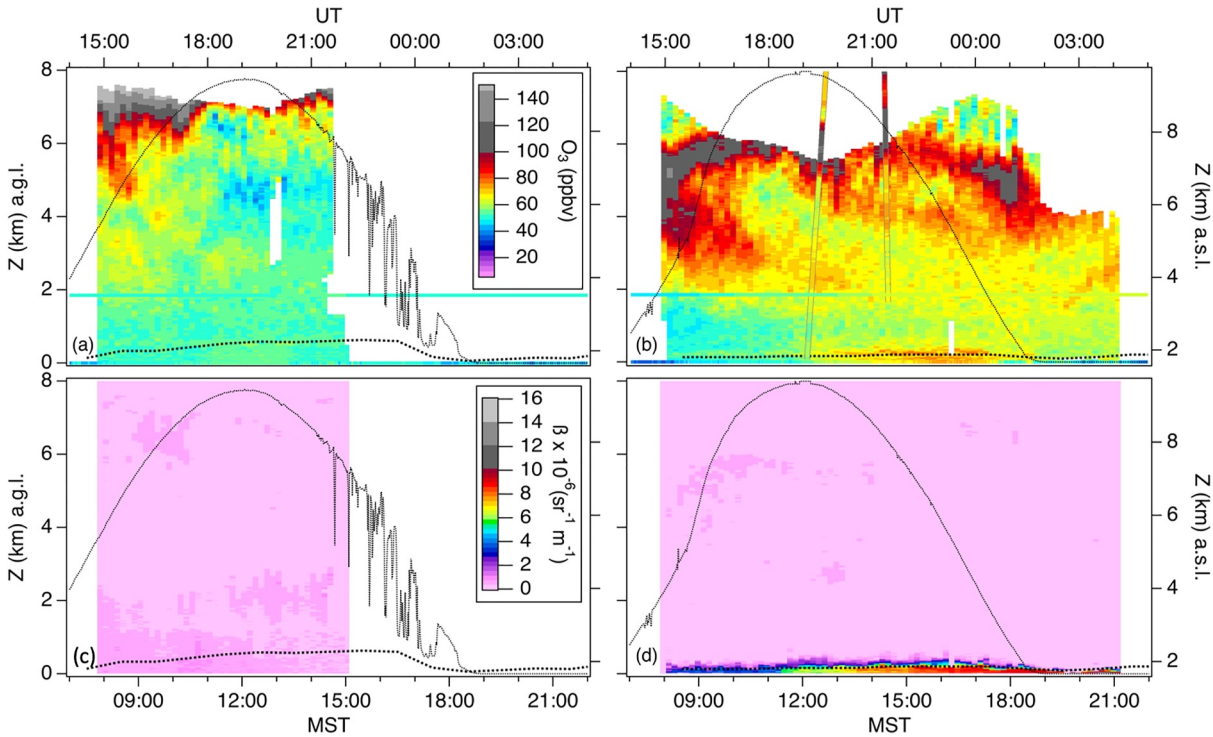

Figure 7. Time-height curtain plots of the O_3 (top) and 0.294 μm backscatter (ß, bottom) distributions measured by TOPAZ on April 14 (left), and April 17 (right). The co-located in situ O_3 measurements are plotted along the bottoms of the upper curtains and the ascending and descending O_3 profiles from the Marshall ozonesonde are superimposed on the O_3 curtain in (b). The black traces show the normalized Longmont Union Reservoir solar irradiance and the dotted curves near the bottom the boundary layer heights inferred from the David Skaggs Research Center Doppler lidar measurements.

monitor located 28 km NNW at an elevation of 3.52 km a.s.l. (1.85 km higher than TOPAZ). The sloping lines in Figure 7b show the ascending and descending profiles from an ozonesonde launched by NOAA GML from the NCAR Marshall Field Site (39.949°N, −105.197, 1.74 km a.s.l.) about 8 km SE of the DSRC at 1207 MST (see Supporting Information S1). The strong westerlies aloft carried the ozonesonde due east (cf. Figure 3b) and the descending profile was measured about 140 km downwind (ESE) of the lidar. The dotted lines near the bottom show the planetary boundary layer (PBL) heights estimated from the co-located Doppler lidar measurements of backscatter, wind shear, and turbulence (Bonin et al., 2017; Choukulkar et al., 2017). The PBL height peaked at 630 m on the 14th, but did not exceed 200 m on the 17th.

The TOPAZ O_3 measurements from April 14 (Figure 7a) show high (>80 ppbv) mixing ratios in the upper troposphere during the morning, but only moderate (40–60 ppbv) mixing ratios later in the day. These mixing ratios and the low tropopause are both consistent with the GEOS-CF analyses in Figure 6. The lidar measurements from April 17 (Figure 7b) show much higher mixing ratios throughout the mid-troposphere with high (>70 ppbv) O_3 measured as low as 3 km a.s.l. The lidar measurements from the afternoon show mixing ratios in excess of 60 ppbv at 2 km a.s.l. That are consistent with both GEOS-CF and the in situ measurements from the three baseline sites (Figure 4b). However, Figure 7b shows a gap between the O_3 aloft and even higher mixing ratios near the surface. The backscatter measurements in Figure 7d also show much higher aerosol near the surface than was measured in the free troposphere on either day.

4.3. Boundary Layer Measurements

Figures 8a and 8c show the hourly-averaged horizontal winds from the Doppler lidar superimposed on the lowest 1 km from the O_3 and ß curtains in Figures 7b and 7d. The plots on the right show the potential temperature (theta), relative humidity (RH), O_3, and wind profiles from the Marshall ozonesonde, and vertical velocity variance profiles from the Doppler lidar. Figure S1 in Supporting Information S1 shows the ozonesonde profiles to 10 km a.g.l. Figure 8a shows that the O_3 mixing ratios at 1 km were similar to the baseline measurements (≈55–60 ppbv) in the morning, but the O_3 and ß near the surface began to increase around 1300 MST, and grew rapidly after the

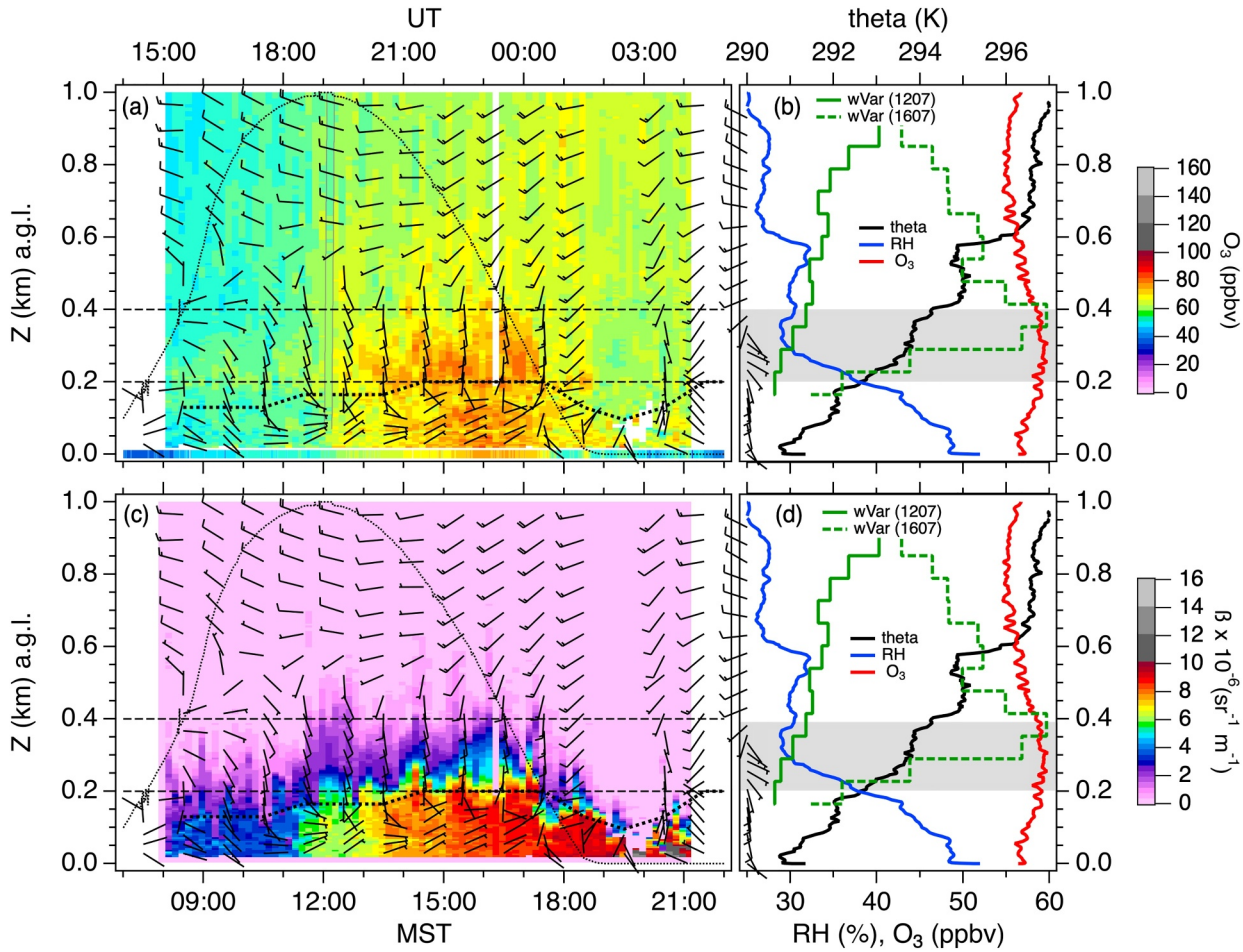

Figure 8. (left) Expanded views of the (top) O_3 and (bottom) ß curtain plots from April 17. The bar along the bottom of the O_3 curtain shows the in situ measurements from the David Skaggs Research Center (DSRC). The barbs show the hourly-averaged winds and the heavy dotted curves the planetary boundary layer heights from the DSRC Doppler lidar. The black dotted curves show the normalized solar flux. (Right) Potential temperature, relative humidity, and wind profiles from the ascending ozonesonde launched at 1207 MST. The solid and dashed green traces show the vertical velocity variance profiles (wVar) from the 1207 and 1607 MST (dashed) Doppler lidar measurements (the scale ranges from 0 to 1 $m^2\ s^{-2}$). The horizontal dashed lines in the curtain plots and gray region in the ozonesonde plots are described in Section 4.3.

northeasterly flow became established in the afternoon. The O_3 and aerosol both decreased after sunset when the low-level winds rotated to the south, but partially recovered when the winds shifted back to the northwest around 2100 MST. The midday sounding (Figures 8b and 8d) shows a rapid decrease in RH within an unusually strong temperature inversion extending from the surface to nearly 400 m. The mean-squared Brunt-Väisälä frequency of $N^2 = 3.7 \times 10^{-4}\ s^{-2}$ within this inversion was comparable to that of the stratosphere [U.S., 1976].

The balloon sounding and the daytime Doppler lidar measurements both show westerly winds above 400 m and easterly to northeasterly winds below 200 m. The region between 200 and 400 m delineated by the dashed lines and gray bands in Figure 8 was characterized by southeasterly to southerly winds. The afternoon Doppler lidar measurements show that there was strong shear-induced turbulent mixing between the top of this transition layer and the lower free troposphere, but very little mixing between the PBL and the bottom of the transition layer. This is consistent with Figure 8c, which shows the highest backscatter was confined to the PBL, and suggests that the elevated O_3 in the transition layer (Figure 8a) was advected to Boulder from the south.

5. Low-Level Transport

The rapid changes in near surface O_3 and ß created by shifts in wind direction (Figure 8) show that low-level transport had a large influence on the April 17 measurements. This is shown more explicitly in Figure 9

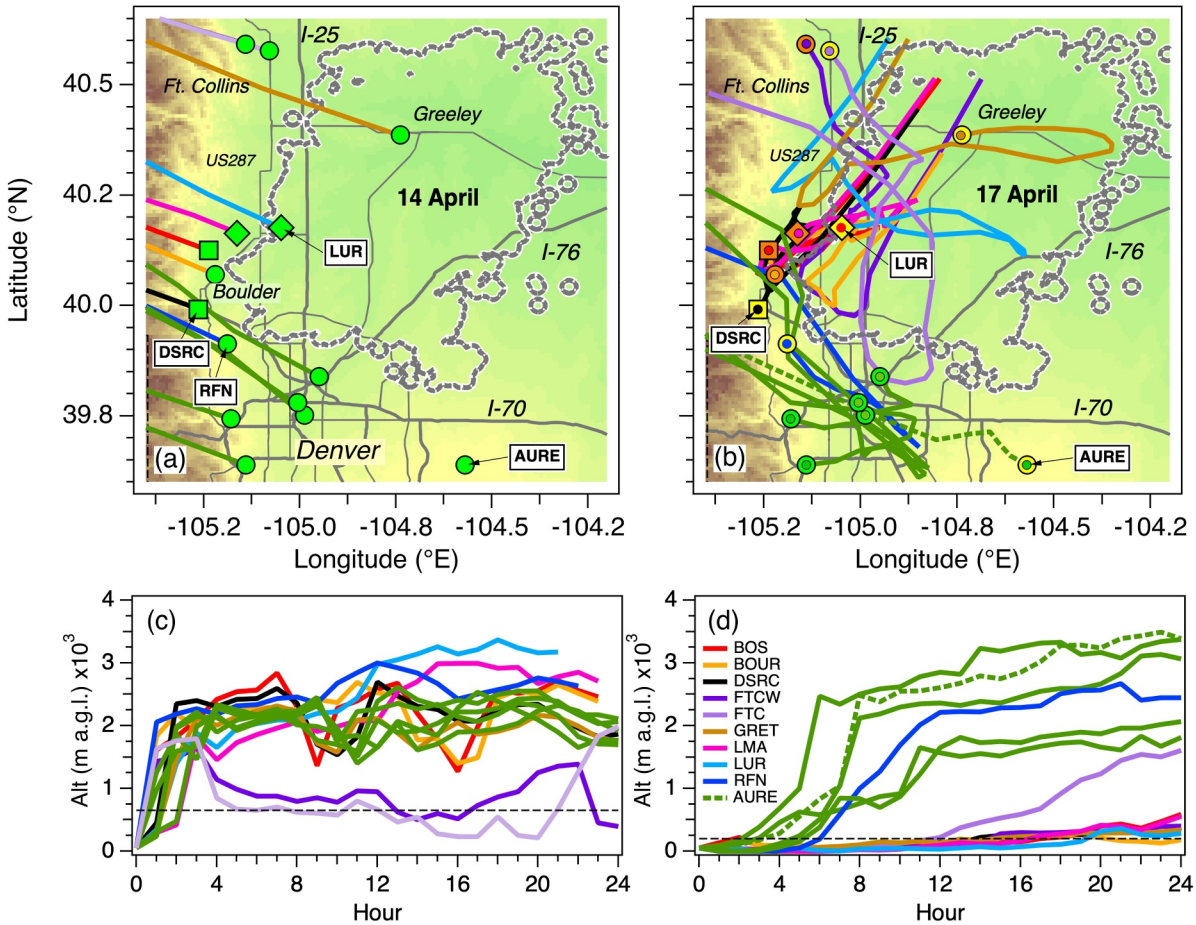

Figure 9. (top) Expanded views of the Northern Front Range showing the MDA8 O_3 measurements (Air Quality Index scale) and 24-hr HYSPLIT back trajectories initialized at 16 MST (23 UT) on April 14 (left) and April 17 (right). The trajectories launched from all of the monitors to the south of Rocky Flats are shown in green. The dark gray lines show the major interstate (thick solid lines) and US highways (thin solid lines). The Wattenberg Gas Field is outlined in dotted gray. (Bottom) Altitude profiles of the 24-hr back trajectories. The horizontal dashed lines show the 630 and 200 m planetary boundary layer heights on the 14th and 17th, respectively.

which displays 24-hr HYSPLIT back trajectories (https://www.ready.noaa.gov/HYSPLIT_traj.php, last access 19 February 2025) (Stein et al., 2015) launched 50 m above each of the O_3 monitors at 1600 MST (2300 UT) on April 14 (left) and April 17 (right). The trajectories were calculated using meteorology from the National Centers for Environmental Prediction 3 km High-Resolution Rapid Refresh model (Benjamin et al., 2016). The top panels show the trajectory horizontal paths and the bottom panels the corresponding altitudes. The trajectories from all of the monitors to the south of Rocky Flats-North (RFN) are plotted in green.

The plots on the left (Figures 9a and 9c) show that nearly all of the trajectories approached the DM/NFR from the west on April 14 and descended rapidly from the lower free troposphere over the Rocky Mountains to the surface. Most of these fast-moving trajectories were more than 800 km to the northwest over southwestern Montana 12 hr earlier (not shown) with the two Ft. Collins trajectories following a lower and more southerly route that passed over Idaho. The plots on the right (Figures 9b and 9d) show that most of the trajectories launched from the monitors to the south of the DSRC on the afternoon of April 17 also descended from the lower free troposphere above the Rocky Mountains, but passed over the Denver metropolitan area before they reached the surface. These parcels doubled back when they encountered the shallow southeasterly upslope flow in the boundary layer, however, and passed slowly through the urban area near the surface. The only exception was the trajectory launched from the rural Aurora East monitor, which descended directly from the free troposphere. Even the trajectory launched from the RFN monitor, which is only 11 km from Boulder, but lies about 150 m higher and over a slight ridge, arrived from the southeast. Figure 9b shows that several of these trajectories passed over the Boulder area as they descended, but were more than 2 km above the surface at the time. In contrast, the trajectories

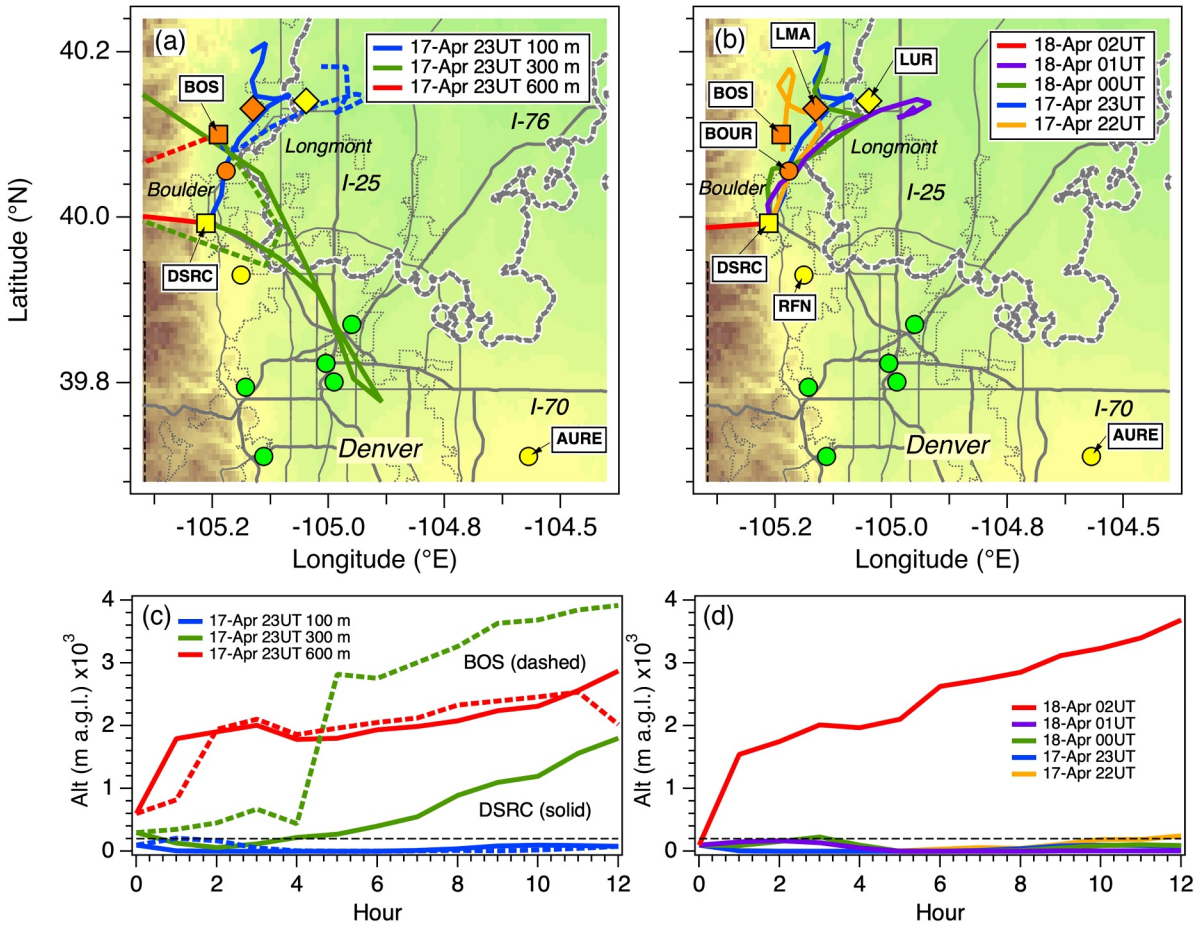

Figure 10. (a) Relief map of the Boulder-Longmont area showing the MDA8 O_3 measurements and 12-hr HYSPLIT back trajectories launched 100, 300, and 600 m above the David Skaggs Research Center (DSRC) (solid) and BOS (dashed) at 1600 MST (2300 UT) on April 17. (b) Same as (a), but showing the back trajectories launched 100 m above the DSRC every hour from 15 to 18 MST (22–01 UT) on the afternoon of April 17. (c) Altitudes of the trajectories shown in (a). (d) Altitudes of the trajectories shown in (b). The dashed line shows the 200 m planetary boundary layer height.

launched from the DSRC and most of the monitors to the north spent the previous 24 hr above the WGF and within a few hundred meters of the surface.

Figure 10a shows 12-hr backward trajectories launched 100, 300, and 600 m above the DSRC and BOS monitors at 1600 MST (2300 UT) on April 17. The DSRC trajectories came from different directions as would be expected from the Doppler lidar winds in Figure 8. Figure 10c shows that the trajectory launched in the lower free troposphere (600 m, red) descended rapidly from the Rocky Mountains to the west, but the trajectory launched in the PBL (100 m, blue), approached the DSRC from the northeast after slowly meandering through the region with the highest O_3 mixing ratios. The 100 and 600 m BOS back trajectories followed similar paths. Both of the intermediate trajectories (300 m, green) approached from the southeast, with the BOS trajectory circling back to the west more than 500 m above Boulder. The DSRC trajectory appears similar to the RFN trajectory in Figure 9b, however, which suggests that the elevated O_3 between 200 and 400 m above the DSRC in Figure 8a may have originated, at least in part, from Denver.

Figure 10b shows a series of back trajectories launched from the DSRC at hourly intervals between 2200 and 0200 UT (1500–1900 MST) on the 17th. The first 4 trajectories arrived from the northeast below 250 m, circling past the monitors with the highest O_3 with the 1600–1800 MST back trajectories passing close to the LUR monitor and I-25, the primary north-south route between Denver and Cheyenne, Wyoming and a major NO_x source, between 5 and 6 hr earlier. The last trajectory (1900 MST or 0200 UT) descended from the west and the lower free troposphere.

6. Photochemical Production

The clear skies, snow-covered ground, weak winds, and shallow boundary layer on 17 April 2020 provided the necessary meteorological conditions for a winter ozone event such as those in the Uinta Basin, and the trajectory analyses in Section 5 show that the highest O_3 mixing ratios were measured in air that had lingered over the western half of the snow-covered WGF earlier in the day. The air sampled by these monitors had thus been exposed to NO_x and VOCs emitted by traffic along I-25 in addition to VOCs from O&NG sources. Motor vehicle exhaust has high concentrations of ethyne as well as the reactive alkenes (e.g., ethene and propene) and aromatics (e.g., benzene and toluene) that contribute to O_3 production in urban areas (Abeleira et al., 2017; Borbon et al., 2013; Broderick & Marnane, 2002; Gentner et al., 2013; Nelson & Quigley, 1984; Thompson et al., 2015).

6.1. NO_x and VOC Measurements

Boulder A.I.R. also measures NO_x, VOCs, and other parameters at the LUR and BOUR monitoring sites (Pollack et al., 2021) (see Supporting Information S1), and the HYSPLIT trajectories in Figure 10 imply that the LUR measurements from the morning of April 17 should be representative of the air sampled by the BOS, BOUR, LMA, and DSRC monitors later that day. NOAA CSL also measured NO_x and VOCs in mid-April as part of an extensive suite of in situ surface measurements conducted during the COVID-AQS study (Peischl et al., 2023; Rickly et al., 2023). Figure 11 compares the (a) O_3, (b) NO_x, (c) carbon monoxide (CO) or carbon dioxide (CO_2), and (d) $PM_{2.5}$ measurements from the LUR, BOUR, and DSRC made between 14 and 19 April. The second snowstorm disrupted the BOUR measurements on April 16–17 so Figure 11a also plots the O_3 measurements from the nearby BOS monitor. The DSRC measurements were also disrupted, but for only a few hours. The mean baseline O_3 from Figure 4b is also plotted, for reference. The DSRC and A.I.R. measurements are described in more detail in the Supporting Information S1.

Figure 12 is similar to Figure 11, but plots the corresponding (a) propane (C_3H_8), (b) *n*-butane (*n*-C_4H_{10}), (c) ethene (C_2H_4), and (d) ethyne/acetylene (C_2H_2) measurements. Note that the DSRC propane and *n*-butane measurements have been scaled up by a factor of 4 to better show the trends. Propane and *n*-butane originate primarily from O&NG activities (Gilman et al., 2013), whereas ethene and ethyne are major components (approximately 10% by weight) of motor vehicle exhaust (Broderick & Marnane, 2002; Gentner et al., 2013; Nelson & Quigley, 1984; Thompson et al., 2015). As in previous studies (e.g. (Gilman et al., 2013)), we use propane and ethyne as tracers for O&NG and motor vehicle (or other combustion) influences, respectively, in our analysis.

The O_3 time series in Figure 11a shows that the measurements from the LUR, BOS, BOUR, and DSRC monitors differed from the baseline mixing ratios by less than ±5 ppbv on the afternoon of the 14th when the HYSPLIT trajectories (Figure 9a) indicate that they all would have sampled free tropospheric air. The peak O_3 mixing ratios differed by as much as 20 ppbv on the afternoon of the 17th, however, with the nearly identical DSRC and LUR measurements lying halfway between the highest O_3 mixing ratios measured by the BOS and BOUR monitors and the baseline mixing ratios from high elevation sites.

In contrast to O_3, Figure 11b shows that the NO_x mixing ratios were much higher at the LUR station than at the DSRC on the 17th. The LUR measurements are dominated by large peaks at 0145 and 0730 MST that are also seen in the CO_2 (Figure 11c), ethene (Figure 12c), and ethyne (Figure 12d) time series, and are mirrored by large decreases in the O_3 time series. The peak NO_x (79 ppbv) and CO_2 (522 ppmv) mixing ratios were the highest recorded during the entire month of April and the timing of the second peak is consistent with morning rush hour traffic. The DSRC measurements show smaller peaks around 0830 MST consistent with this interpretation. The LUR measurements also show smaller peaks on the mornings of the 14th, 15th, and 18th which confirms that the unusually high concentrations on the 17th were caused by the exceptionally shallow inversion layer which trapped more of the emissions near the surface. The LUR monitoring station is located 6 km west of I-25, the primary north-south route between Denver and Cheyenne. Figures 11 and 12 show that the motor vehicle emissions decreased when the winds shifted to the northwest at sunrise, and the concentrations of propane (Figure 12a) and *n*-butane (Figure 12b) increased. This may reflect the influence of a nearby (0.3 km) O&NG well that was active in April 2020, but has since been decommissioned.

The scatter plots in Figure 13 compare the LUR *n*-butane, propane, ethene, and ethyne measurements from April, 16–18, 2020 with the relationships found in earlier WGF studies by Gilman et al. (2013) and Pollack et al. (2021).

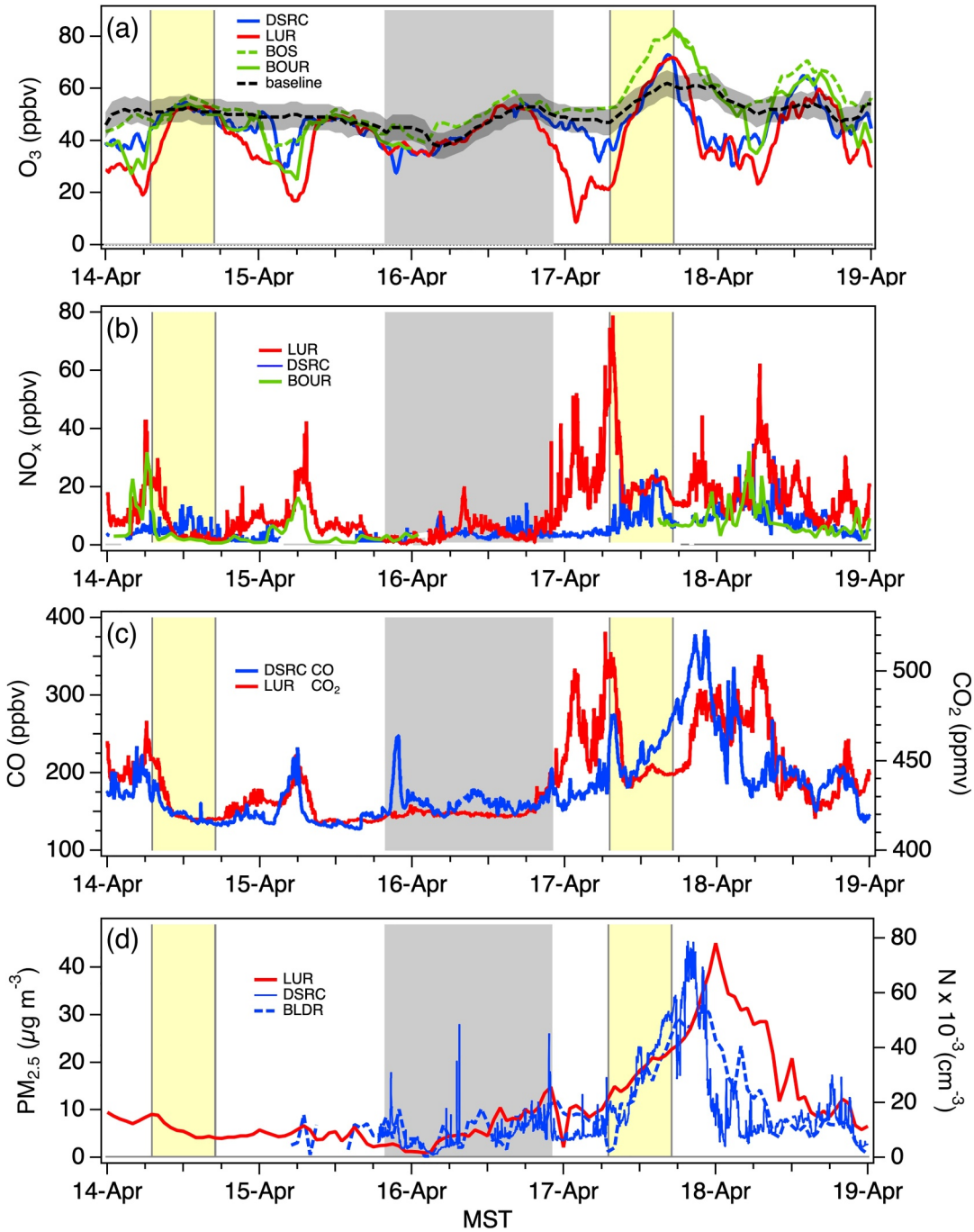

Figure 11. Time series of (a) O_3, (b) NO_x (c), CO (David Skaggs Research Center (DSRC)), and CO_2 (Longmont Union Reservoir (LUR)), and (d) $PM_{2.5}$ measurements from the LUR (red), Boulder Reservoir (green), and DSRC (blue) stations. The mean baseline O_3 (±5 ppbv) and BOS (dashed green) measurements are also plotted in (a). Panel (d) shows both the particle number density measured by the ultra-high sensitivity aerosol spectrometer at the DSRC and the mass concentrations from the LUR station and the regulatory monitor in downtown Boulder. Snow periods are highlighted in gray and the photochemically active periods on the 14th and 17th in yellow.

The solid lines show the orthogonal distance regression (ODR) fits to the measurements. The measurements from the morning (0000–1200 MST) of April 17 are highlighted in red. The dotted lines in Figures 13a and 13d show the emission ratios derived by Gilman et al. (2013) who applied multivariate regression analysis (MVR) to an extensive suite of VOC measurements made at the nearby Boulder Atmospheric Observatory (BAO) during the

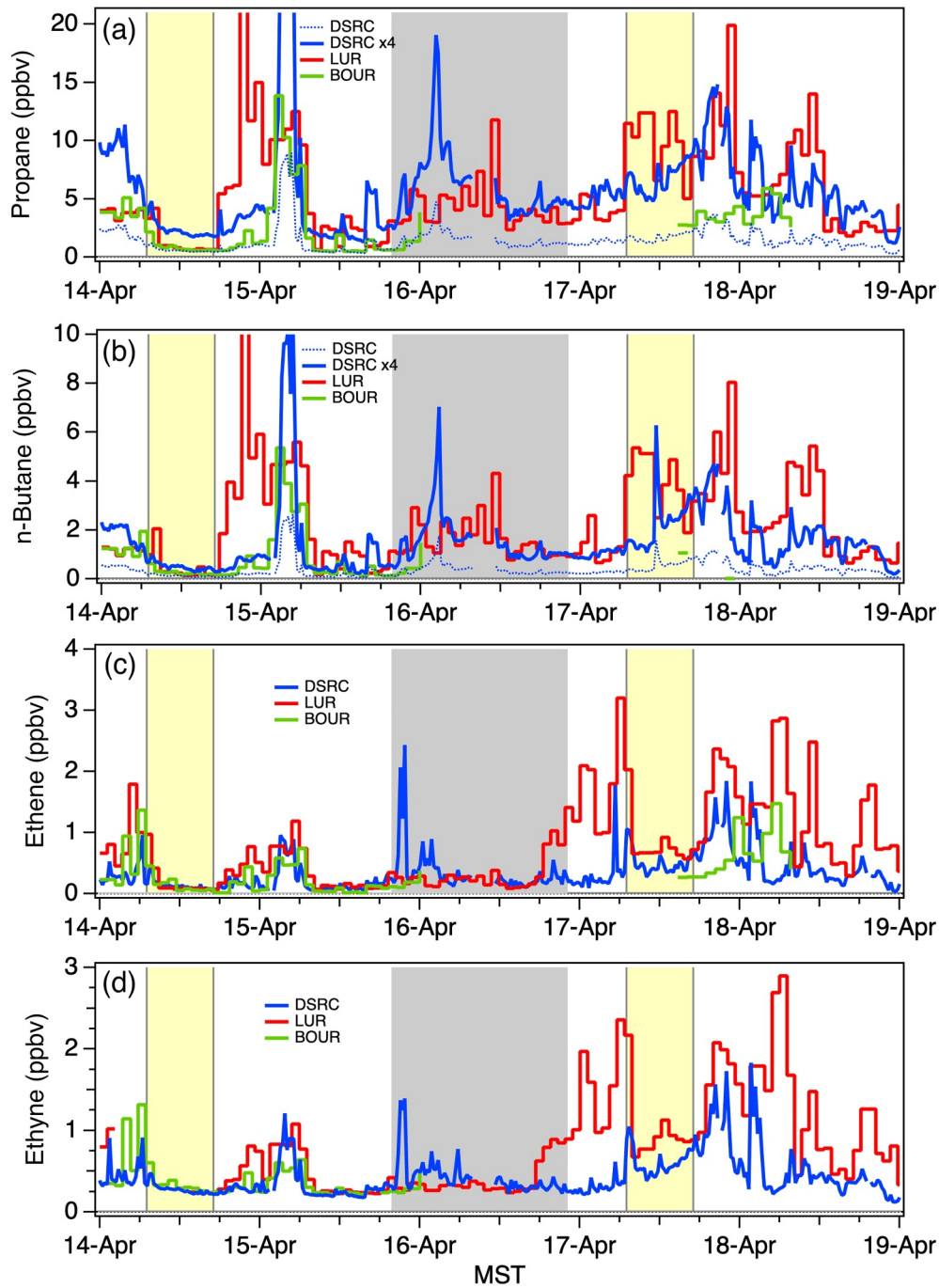

Figure 12. Same as Figure 11, but showing the corresponding: (a) C_3H_8, (b) n-C_4H_{10}, (c) C_2H_4, and (d) C_2H_2 measurements. The David Skaggs Research Center C_3H_8 and n-C_4H_{10} measurements have been scaled up by a factor of 4. Snow periods are highlighted in gray and the photochemically active periods on the 14th and 17th in yellow.

NACHTT (Nitrogen, Aerosol Composition, and Halogens on a Tall Tower) campaign (18 February–7 March 2011) (Brown et al., 2013). The dashed lines show the emission ratios from Pollack et al. (2021) who analyzed winter (December-February; DJF) and spring (March–May; MAM) measurements made at the BOUR between 2017 and 2019 using both MVR and positive matrix factorization analysis (PMF) [Pollack et al., 2021]. As was seen in those studies, Figures 13a and 13b show that n-butane was highly correlated ($R^2 = 0.87$) with propane, but uncorrelated ($R^2 = 0.04$) with ethyne, whereas Figures 13c and 13d show that ethene was uncorrelated ($R^2 = 0.04$) with propane, but highly correlated ($R^2 = 0.92$) with ethyne as seen in the earlier studies. The slope of the ODR fit

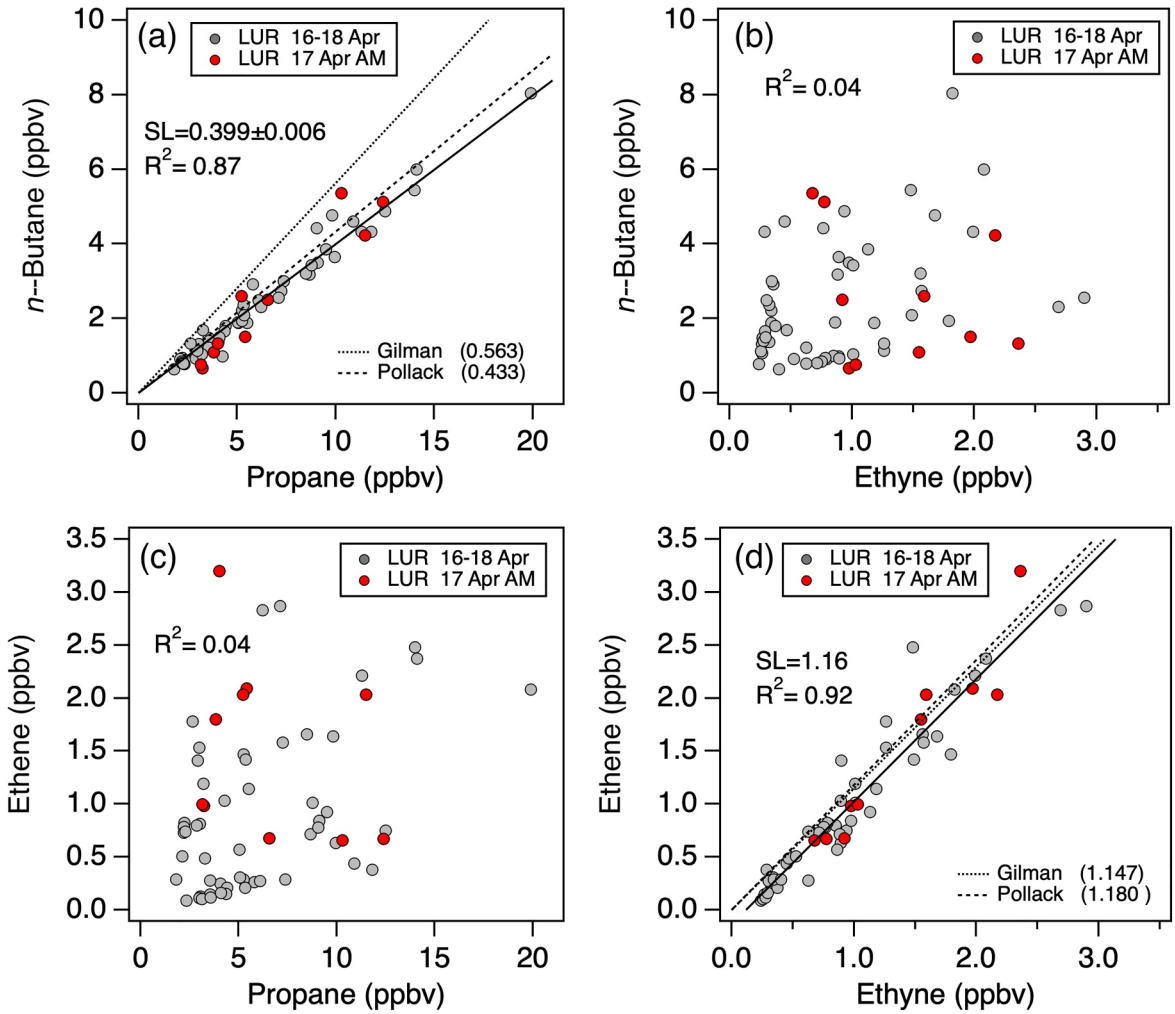

Figure 13. Scatter plots comparing the Longmont Union Reservoir *n*-butane (top) and ethene (bottom) measurements to the propane (left) and ethyne (right) concentrations. The filled gray circles show all of the measurements made from April 16–18. The solid lines show the orthogonal distance regression regression fits to these measurements and the dotted lines the emission ratios from Gilman et al. (2013). The dashed lines show the winter (DJF) emission ratios from Pollack et al. (2021). The filled red circles highlight the measurements from the afternoon and evening (1200–2100 MST) of April 17 when the highest O_3 was measured.

(0.399 ± 0.006) in Figure 13a is smaller than that seen at the BAO nearly 10 years earlier, but comparable to that found in the more recent BOUR winter measurements. The slope in Figure 13d is similar to that found in both of the earlier studies.

The DSRC measurements in Figures 11 and 12 appear both quantitatively and qualitatively different from the LUR measurements with most of the time series showing a nearly exponential buildup ($t \approx 8$ hr) on April 17 consistent with the transport of co-mingled traffic and O&NG emissions from Longmont, I-25, and the WGF implied by the HYSPLIT back trajectories in Figure 10. This co-mingling is shown by Figure 14, which is similar to Figure 13, but shows the DSRC measurements. The filled red circles highlight the measurements from the afternoon and evening (1200–2100 MST) of April 17 when the highest O_3 was measured. The solid red lines show the ODR fits to these measurements, and the solid, dotted, and dashed black lines are the same as in Figure 13. In contrast to Figures 13b and 13c, Figures 14b and 14c show significant correlations between *n*-butane and ethyne (Figure 14b), and between ethene and propane (Figure 14c) at the DSRC, particularly on the afternoon and evening of the 17th (red points).

The relative contributions of motor vehicles and O&NG sources to the VOC burden can also be estimated from the relative abundances of the pentane isomers (Gilman et al., 2013). Raw natural gas samples collected near O&NG facilities in the WGF have a mean *i*-pentane/*n*-pentane ratio of 0.86 ± 0.02 (LT Environmental, 2007), but

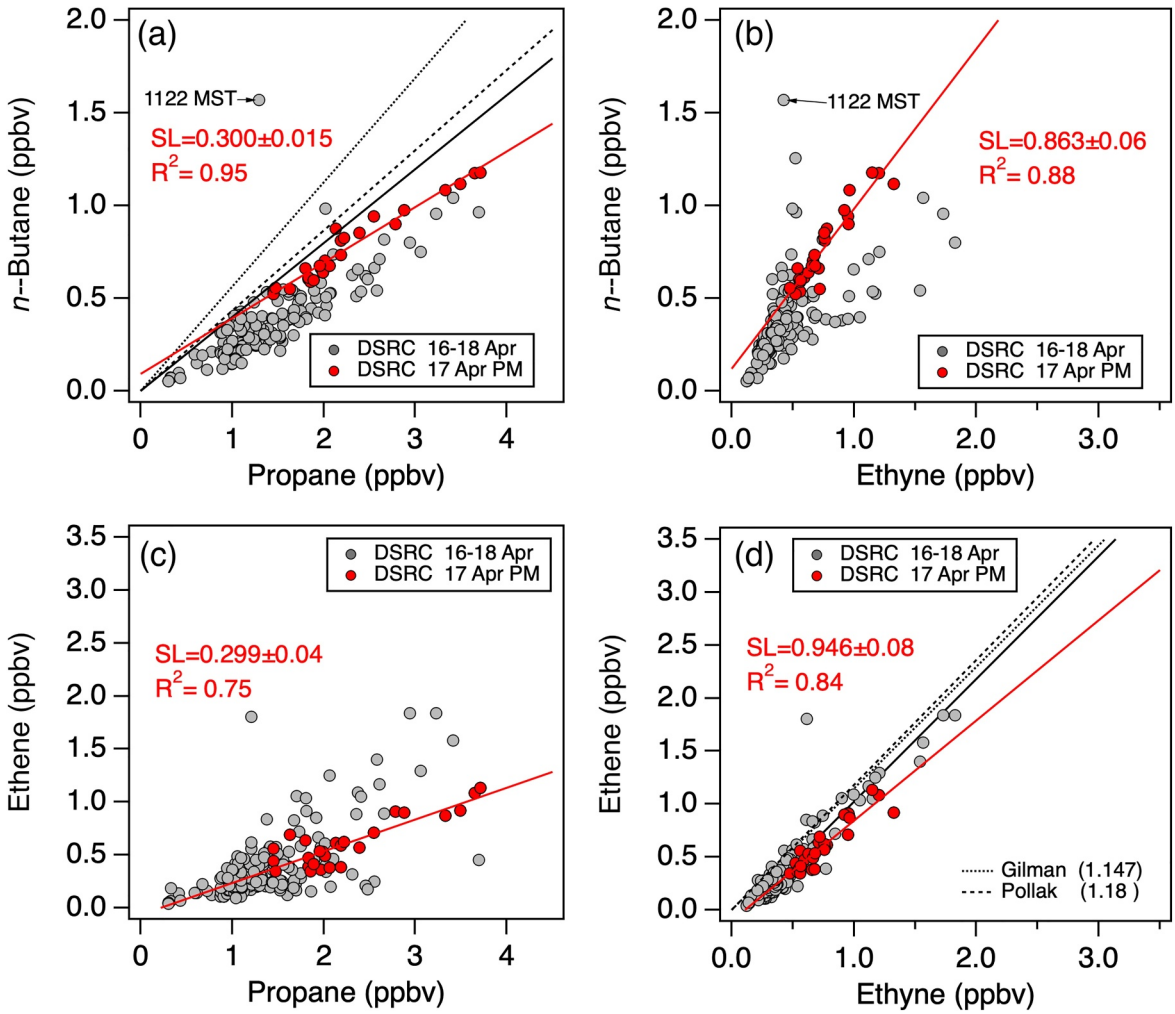

Figure 14. Same as Figure 13, but for the David Skaggs Research Center with the afternoon (MST) measurements from the 17th highlighted. Note the different scales. The solid red lines are the orthogonal distance regression fits to the afternoon and evening (1200–2100 MST) measurements from the 17th, which are plotted in red. The solid, dashed, and dotted lines are from Figure 13.

gasoline is enriched in *i*-pentane compared to raw natural gas (Gentner et al., 2009) and the *i*-pentane/*n*-pentane ratio in air samples from heavily trafficked areas typically lie between 2 and 3 (Rossabi & Helmig, 2018). Figures 15a and 15b, which are similar to Figure 2 of Gilman et al. (2013), compare the isomeric pentane measurements from the LUR and DSRC, respectively, with the mean values from previous studies. The solid lines correspond to the WGF raw natural gas ratio of 0.86 and the dotted lines the ratio of 2.41 ± 0.02 derived from measurements made in Pasadena, CA as part of the CalNex campaign (June-July 2010) (Borbon et al., 2013).

The other lines are from previous studies in the Boulder-Longmont area and range from the long dash line corresponding to the values of 0.885 ± 0.002 and 0.89 ± 0.01 derived from the winter measurements at the BAO (Gilman et al., 2013) and BOUR (Pollack et al., 2021), to the short dash line (1.10 ± 0.05) derived from two days of measurements at the DSRC in September 2010. The dot-dash line shows that the mean ratio of 0.965 derived from measurements made at multiple sites in the Longmont area between March and June of 2013 lies between these values (Thompson et al., 2015). All of these ratios show a much larger O&NG influence in the Boulder-Longmont area as do nearly all of the measurements from the LUR and DSRC plotted in Figure 15. The LUR only measurements showing significant motor vehicle influences are the two points corresponding to the two large traffic peaks (0140 and 0712 MST) in the morning LUR measurements (cf. Figures 11 and 12) and the spikes at 1122 and 1142 MST attributed to snow removal operations at the DSRC.

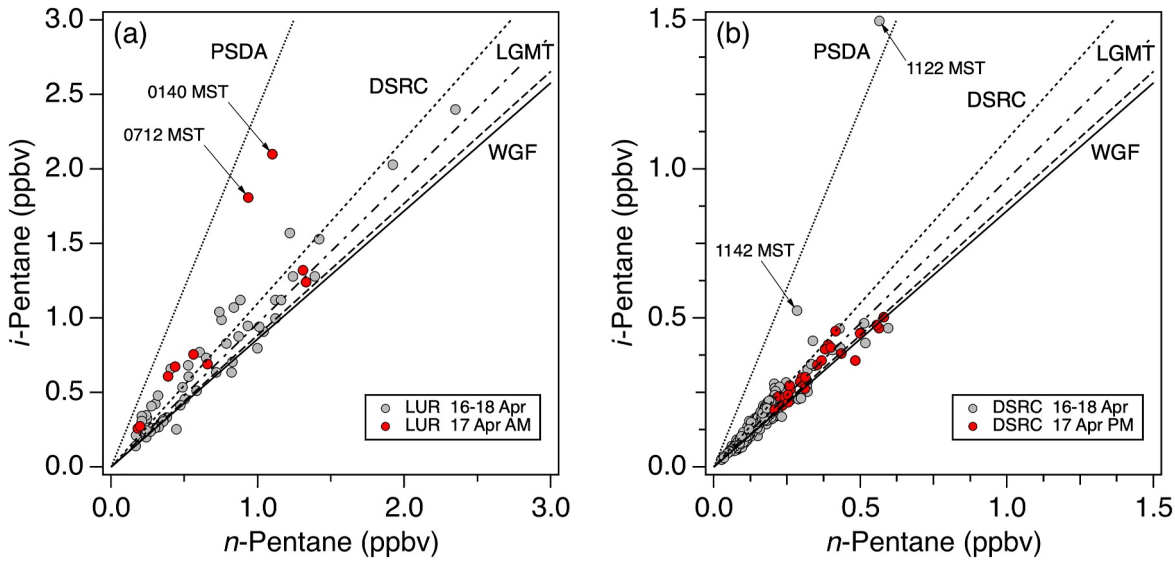

Figure 15. Scatter plots comparing the *i*-pentane and *n*-pentane measurements from the (a) Longmont Union Reservoir and (b) David Skaggs Research Center (DSRC). Note the different scales. The solid line shows the mean slope (0.86) derived from Wattenberg Gas Field natural gas samples. The dot, long dash and short dash lines show relationships derived from previous measurements at Pasadena (PSDA), the Boulder Atmospheric Observatory, and DSRC (Gilman et al., 2013). The dot-dashed line is from measurements in the Erie/Longmont area by Thompson et al. (2015).

6.2. OH Reactivity

The production of O_3 in the boundary layer is driven primarily by photolysis of NO_2 formed in the reaction of peroxy radicals (ROO•) with NO. The peroxy radicals are formed through a sequence initiated by the reaction of VOCs with the OH• radical and the "total OH reactivity" is often used as a measure of the O_3 production potential (Gilman et al., 2013). This quantity is calculated as:

$$R_{OH+VOC} = \sum(k_{OH+VOC} \times [VOC]) \quad (1)$$

where $k_{OH + VOC}$ is the temperature and pressure dependent rate constant for the reaction with OH (Atkinson, 1986, 2003). Figure 16a plots the total OH reactivity calculated using the LUR measurements and a mean temperature of 278 K (5°C). The total reactivity ranged from 0.12 s^{-1} on the afternoon of the 14th when the station was exposed to free tropospheric air, to 7.6 s^{-1} when the winds subsided later that night. Note that these totals do not include the mean contribution of 0.27 s^{-1} calculated for CH_4, which varied little from day-to-day. The total reactivity is also resolved into the contributions from O&NG, urban, and biogenic sources, where we assume that O&NG operations were the primary source of C_2-C_8 alkanes and C_5–C_8 cycloalkanes, urban activities (motor vehicles, residential, and commercial heating, power generation, and industrial activities) the primary sources of ethyne, C_6–C_8 aromatics, and alkenes, and biogenic emissions which are the primary source of isoprene and pinene. The latter, which are important during summer, were negligible during this study. The concentrations of ethane, which was the most abundant VOC in both the LUR and DSRC measurements and is the second largest component of raw natural gas after methane, but also a major component of tailpipe emissions (Gentner et al., 2009), were resolved into the O&NG and urban contributions using the relationships from Gilman et al. (2013) and the measured propane and ethyne.

Figure 16a shows that O&NG emissions made the largest contributions to the total OH reactivity with the much higher alkane concentrations more than compensating for the greater reactivity of the alkenes emitted by motor vehicles. Previous studies in the area (Abeleira et al., 2017; Gilman et al., 2013; Swarthout et al., 2013) reached similar conclusions. The highest VOC concentrations were usually measured at night and Figure 16b plots the reactivities scaled by the relative LUR solar flux to emphasize the differences in photochemical activity on the clear (14th and 17th) and cloudy (15th, 16th, and 18th) days. Figure 16a shows that the total reactivity of 1.7 s^{-1} at local noon on the 17th was more than an order of magnitude larger than the 0.12 s^{-1} at local noon on the 14th despite the similar solar fluxes. This is about half the mean value of 3 s^{-1} estimated from the wintertime

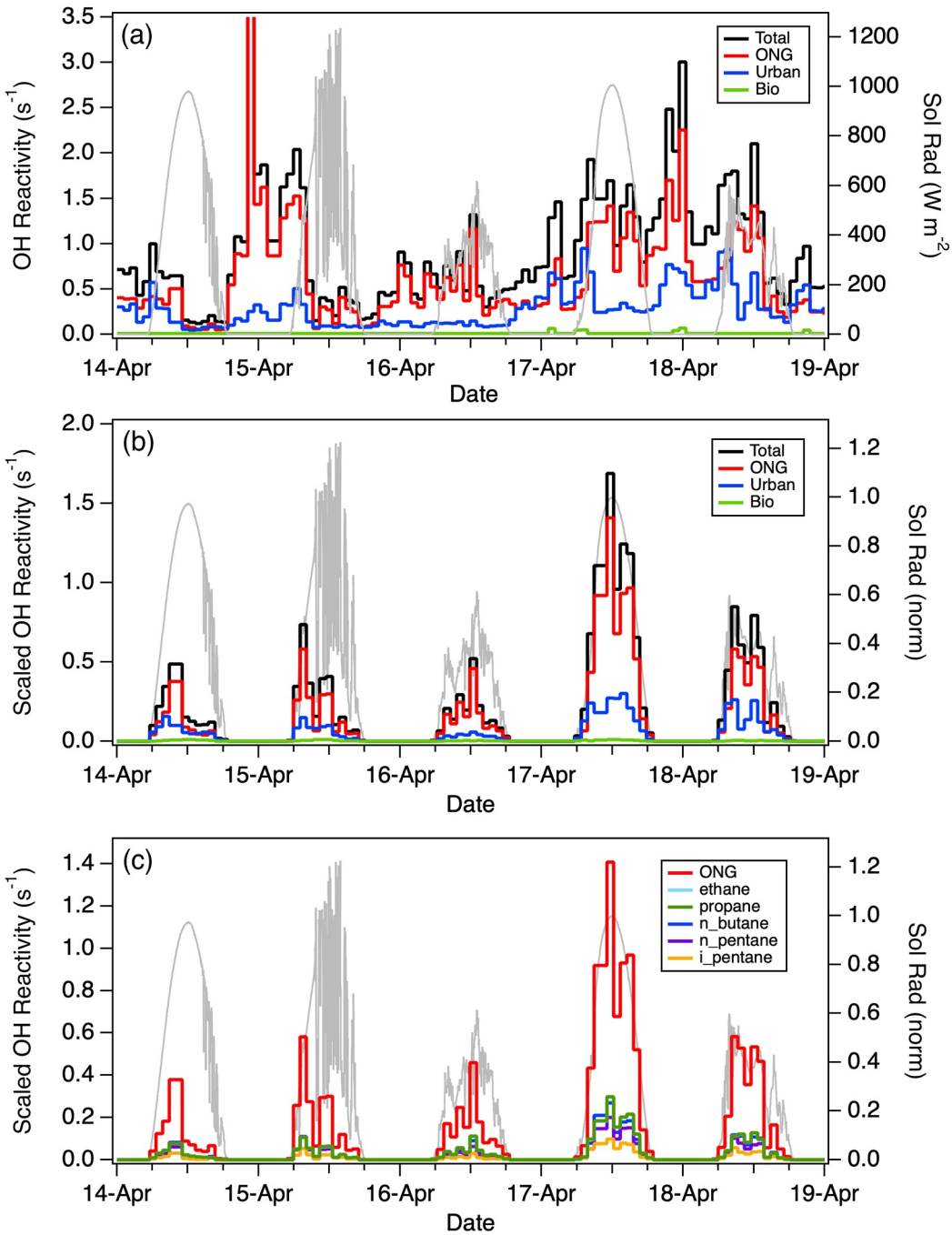

Figure 16. Calculated OH reactivities for the non-methane volatile organic compounds measured at Longmont Union Reservoir. (a) Total reactivity resolved into the contributions from O&NG, urban, and biogenic sources. (b) Same as (a), but normalized by the peak solar flux on April 17. (c) Same as (b), but showing the contributions of the individual alkanes to the O&NG total.

measurements at the BAO (Gilman et al., 2013; Swarthout et al., 2013). Figure 16c is similar to Figure 16b, but shows the contributions of the individual VOCs to the O&NG total. The largest contributions were from propane, ethane, *n*-butane, and *n*-pentane; the propane and ethane contributions are nearly identical and not easily distinguished in the figure. Our estimates do not include the contributions of formaldehyde, acetaldehyde, or other OVOCs (Section 6.3) that were not measured at LUR, but accounted for approximately 25% of the total reactivity

in those studies. Ethanol (C_2H_5OH), which comprises about 10% of Colorado winter gasoline (de Gouw et al., 2012), was the second most abundant VOC at the DSRC, but has low ozone forming potential.

6.3. Chemical Box Model

The shallow boundary layer and weak winds on April 17 created the ideal conditions for the application of a chemical box model (Edwards et al., 2014). Here, we use the "Framework for 0-D Atmospheric Modeling (F0 a.m.)" box model (Wolfe et al., 2016) with the more extensive suite of VOCs, OVOCs, and other compounds (see Supporting Information S1) measured at the DSRC during the spring and summer of 2020 as part of COVID-AQS (Peischl et al., 2023). Our application closely follows that of Rickly et al. (Rickly et al., 2023) who used the F0AM model with the same measurement suite to investigate the impact of wildfire smoke on O_3 production in Boulder during the late summer and early fall of 2020. As in that study, the meteorological inputs including pressure, temperature, and RH, were obtained either from local measurements or WRF-Chem, and the boundary layer height and low-level winds were taken from the Doppler lidar measurements at the DSRC. We use the NWR measurements (cf. Figure 4) as a proxy for the baseline O_3 in the lower free troposphere, and the NOAA GML Solar Position Calculator (https://gml.noaa.gov/grad/solcalc/azel.html, last access 19 February 2025) to calculate the solar zenith angle.

Figure 17a compares the DSRC, NWR, and BOS measurements from April 14–18 with the O_3 mixing ratios calculated by the box model for the periods with no active precipitation. The solid red line shows the mixing ratios calculated when all of the available DSRC VOC measurements are included, and the dashed red line the mixing ratios calculated when only the measurements of those VOCs (alkanes, alkenes, and the BTEX compounds, i.e., benzene, toluene, and xylenes) compounds that were also measured at the LUR and BOUR monitoring sites are included. The similarity between the two model runs and the DSRC, NWR, and BOS measurements from April 14–15 confirms that there was very little net photochemical production of O_3 on those days. The runs diverge on April 17, however, with the solid red line closely following the DSRC measurements, whereas the dashed red line drops below the measured values. These differences show the important role of oxygenated VOCs in the O_3 production on April 17–18.

Figure 17b is similar to 17a, but shows the box model results for the LUR monitoring site with the dashed red line calculated from the LUR NO_x and VOC measurements in Figures 11 and 12. We were unable to apply the box model to the measurements from the BOUR monitoring site since this station was offline for most of the high O_3 episode (cf. Figures 11 and 12). As seen in Figure 17a, this limited VOC measurement suite cannot reproduce the observations. This simulation uses the PBL heights measured at the DSRC since there were no independent measurements of this quantity near the LUR monitoring site, and the failure of the model to reproduce the deep early morning minima in Figure 17b shows that the assumed values overestimate the depth of the nocturnal inversion layer.

The box model simulations show that the O_3 production on April 17–18 was driven by photolysis of formaldehyde, acetaldehyde, and other oxygenated compounds that acted as radical amplifiers. This was also found to be the case in the Uinta Basin (Edwards et al., 2014) and a recent analysis (Dix et al., 2023) of measurements from the Shale Oil and Natural Gas Nexus (SONGNEX) aircraft campaign concluded that 96 ± 3% of the above background formaldehyde in the Uinta Basin, Denver-Julesburg Basin, and 7 other O&NG fields sampled during March and April 2015 was a secondary product formed by photooxidation of the primary VOC emissions. The more populated parts of the DM/NFR have other potential sources of formaldehyde, however, including direct emissions from motor vehicles, power plants, residential/commercial heating systems, and other combustion sources (Bastien et al., 2019; Green et al., 2021), but Figure 18 shows that the CH_2O mixing ratios measured at the DSRC on April 17 were much more strongly correlated with n-C_4H_{10} than with C_2H_2 and C_2H_4, suggesting that most of this formaldehyde was also derived from O&NG sources. The weaker correlations with C_2H_2 and C_2H_4 in Figures 18b and 18c can also be explained by the mingling of urban and O&NG emissions as was seen in Figure 14. Figure 18a also shows that CH_2O and n-C_4H_{10} were essentially uncorrelated in the measurements from April 14–16, confirming that the formaldehyde was not a primary emission.

The 17 April 2020 high O_3 episode occurred early in the COVID-19 lockdown when motor vehicle traffic and the associated NO_x emissions were greatly reduced (Harkins et al., 2021). The NO_x sensitivity tests in Figure 19 show that there was still more than enough NO_x available to push O_3 production into the NO_x-saturated regime on both the 14th and 17th, however, in contrast to the model runs conducted later that summer which found the O_3

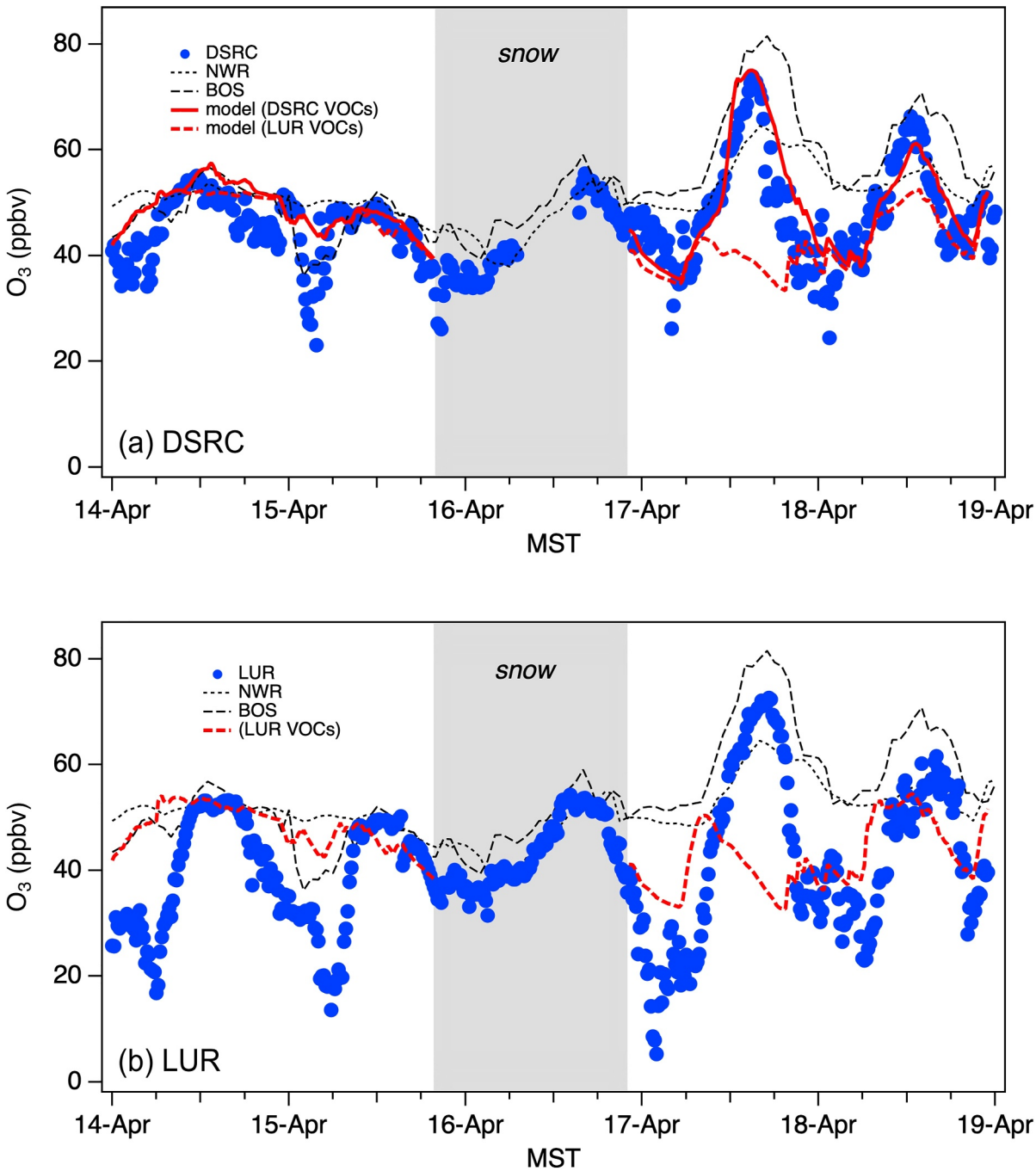

Figure 17. (a) Measured (filled blue circles) and simulated (solid and dashed red lines) O_3 at the David Skaggs Research Center (DSRC). The solid line uses all of the DSRC volatile organic compound (VOC) measurements, while the dashed line uses only those for VOCs that were also measured at Longmont Union Reservoir (LUR). The BOS (long-dashed black) and Niwot Ridge (short-dashed black) measurements are included for comparison. (b) Same as (a), but for LUR.

production to be NO_x-sensitive (Rickly et al., 2023). This difference may be due in part to the absence of isoprene and other highly reactive biogenic VOCs during late winter and early spring. The traffic counts along the stretch of I-25 nearest the LUR monitor and US 36, which connects Denver with Boulder and passes within 2 km of the DSRC, in April 2020 were down to about 35% and 45% of the April average for 2017–2019 (https://dtdapps.coloradodot.info/otis, last access 19 February 2025), and if we assume that the NO_x emissions decreased by a similar amount, the sensitivity curves in Figure 19 suggest that the O_3 production on the 17th would have been

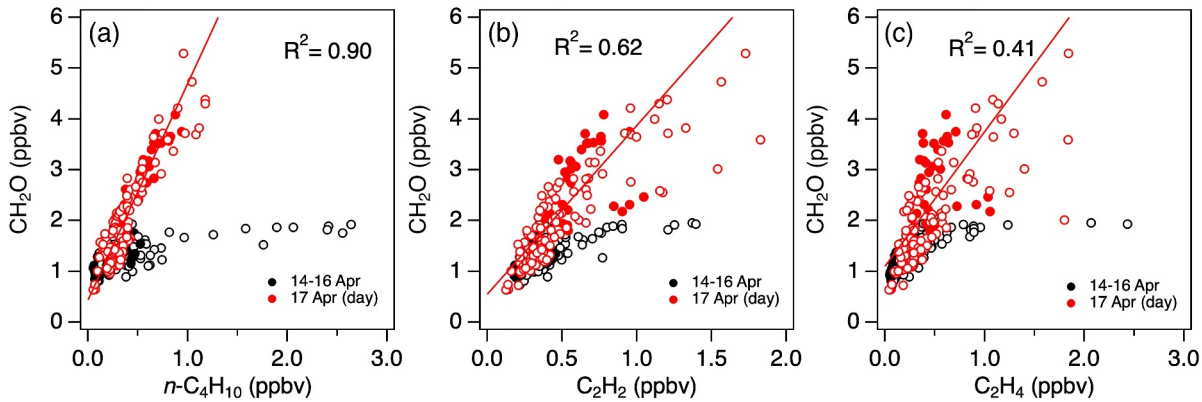

Figure 18. Scatter plots comparing the CH_2O mixing ratios measured at the David Skaggs Research Center on April 14–16 (black) and April 17–18 (red) with the co-incident measurements of (a) *n*-butane, (b) ethyne, and (c) ethene. The orthogonal distance regression fits and correlation coefficients are for the April 17 daytime measurements (0700–1700 MST) represented by the filled red circles. The 30-s PTR-MS measurements have been interpolated to match the longer integration time of the whole air sampler.

about 30% smaller (open squares) than was measured in 2020 (filled squares) without the COVID-19 quarantine and the NAAQS exceedances probably would not have occurred.

7. Summary and Conclusions

The high O_3 event that occurred along the Northern Front Range of Colorado on 17 April 2020 was in many ways similar to the wintertime O_3 events endemic to the Uinta Basin of northeastern Utah and Upper Green River Basin of southwestern Wyoming. Like those events, the photochemical production and accumulation of O_3, $PM_{2.5}$, and other pollutants was caused by the buildup of NO_x and VOCs from anthropogenic sources within an extremely shallow boundary layer combined with clear skies and snow cover to increase the surface albedo and hence the effective solar flux. Similar to those events, the reactive VOCs appear to have originated primarily from O&NG activities, but in this case the NO_x appears to have come primarily from motor vehicles rather than the combustion sources associated with the O&NG industry (e.g., drilling rigs, compressors, pumping stations, etc.). If so, the event appears to have been exacerbated by the decrease in NO_x that followed the reduction in motor vehicle traffic

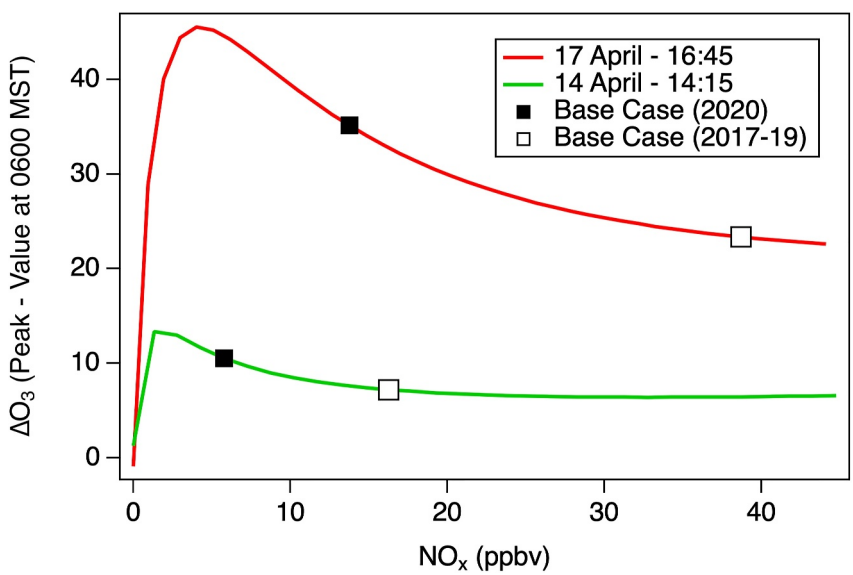

Figure 19. Nitrogen oxides (NOx) sensitivity curves from the chemical box model calculations for April 14 and 17. The filled squares show the O_3 production calculated from the 1000 to 1600 MST mean NO_x. The open squares show the production expected if the NO_x were doubled to reflect 2019 traffic volumes.

during the COVID-19 quarantine. This implies that similar winter events might become more common in the Colorado Northern Front Range as emissions controls reduce NO_x levels through the transition region of O_3-NO_x sensitivity, even though recent box-model analyses suggest that such NO_x reductions may mitigate summertime O_3 in the region. A search through the previous 10 years of CDPHE measurements found no obvious examples of similar episodes, but NO_x has been steadily decreasing in the DM/NFR over the last two decades (Langford et al., 2022) resulting in higher VOC/NO_x ratios and possibly leading to more of these early season ozone events in future. Indeed, another high winter O_3 event occurred less than one year later on March 19-20, 2021 (Caputi et al., 2025). Unfortunately, the ozone lidar and COVID-AQS in situ measurements used in the present study were not available for an analysis comparable to that described here.

Data Availability Statement

The regulatory O_3 measurements used in this study are available at https://www.epa.gov/outdoor-air-quality-data (last access 19 February 2025). The A.I.R. monitoring data have been submitted to EBAS (https://ebas.nilu.no/). The NOAA COVID-AQS data are available at https://csl.noaa.gov/groups/csl7/measurements/2020covid-aqs/ (last access 19 February 2025) and the TOPAZ lidar data at https://tolnet.larc.nasa.gov/ (last access 19 February 2025). The MERRA-2 and WRF-Chem images were downloaded from the publicly accessible archives at https://fluid.nccs.nasa.gov/reanalysis/classic_merra2/ (last access 19 February 2025) and https://www.acom.ucar.edu/firex-aq/forecast.shtml (last access 19 February 2025), respectively. The HYSPLIT back trajectories were calculated using the online READY model (https://www.ready.noaa.gov/HYSPLIT_traj.php, last access 19 February 2025).

Acknowledgments
The authors would like to thank Catherine Burgdorf-Rasco for creating and maintaining the CSL data archive. We would also like to thank Scott Landes, Dan Welsh, and Erick Mattson of the Colorado Department of Public Health and the Environment for help with the monitoring data, and Audra McClure-Begley for collecting and archiving the NOAA GML data. The NOAA CSL TOPAZ lidar operations were supported in part by the NASA-sponsored Tropospheric Ozone Lidar Network (TOLNet). The monitoring of meteorological and chemical atmospheric data by Boulder A.I.R. was funded by the City of Longmont and Boulder County. Resources supporting the GEOS-CF model simulations were provided by the NASA High-End Computing (HEC) Program through the NASA Center for Climate Simulation (NCCS) at Goddard Space Flight Center. The WRF-Chem simulations are based upon the work supported by the NSF National Center for Atmospheric Research, which is a major facility sponsored by the NSF under Cooperative Agreement No. 1852977. The Cooperative Institute for Research in Environmental Sciences (CIRES) employees were supported in part by NOAA cooperative agreements NA17OAR4320101 and NA22OAR4320151. The scientific results and conclusions, as well as any views or opinions expressed herein, are those of the author(s) and do not necessarily reflect the views of NOAA or the Department of Commerce.

References

Abeleira, A., Pollack, I. B., Sive, B., Zhou, Y., Fischer, E. V., & Farmer, D. K. (2017). Source characterization of volatile organic compounds in the Colorado northern front range metropolitan area during spring and summer 2015. *Journal of Geophysical Research: Atmospheres*, *122*(6), 3595–3613. https://doi.org/10.1002/2016jd026227

Ahmadov, R., McKeen, S., Trainer, M., Banta, R., Brewer, A., Brown, S., et al. (2015). Understanding high wintertime ozone pollution events in an oil- and natural gas-producing region of the Western US. *Atmospheric Chemistry and Physics*, *15*(1), 411–429. https://doi.org/10.5194/acp-15-411-2015

Alvarez II, R. J., Senff, C. J., Langford, A. O., Weickmann, A. M., Law, D. C., Machol, J. L., et al. (2011). Development and application of a compact, tunable, solid-state airborne ozone lidar system for boundary layer profiling. *Journal of Atmospheric and Oceanic Technology*, *28*(10), 1258–1272. https://doi.org/10.1175/Jtech-D-10-05044.1

Atkinson, R. (1986). Kinetics and mechanisms of the gas-phase reactions of the hydroxyl radical with organic-compounds under atmospheric conditions. *Chemical Reviews*, *86*(1), 69–201. https://doi.org/10.1021/cr00071a004

Atkinson, R. (2003). Kinetics of the gas-phase reactions of OH radicals with alkanes and cycloalkanes. *Atmospheric Chemistry and Physics*, *3*(6), 2233–2307. https://doi.org/10.5194/acp-3-2233-2003

Bader, D. C., & McKee, T. B. (1985). Effects of shear, stability and valley characteristics on the destruction of temperature inversions. *Journal of Climate and Applied Meteorology*, *24*(8), 822–832. https://doi.org/10.1175/1520-0450(1985)024<0822:Eossav>2.0.Co;2

Bastien, L. A. J., Brown, N. J., & Harley, R. A. (2019). Contributions to local- and regional-scale formaldehyde concentrations. *Atmospheric Chemistry and Physics*, *19*(13), 8363–8381. https://doi.org/10.5194/acp-19-8363-2019

Benjamin, S. G., Weygandt, S. S., Brown, J. M., Hu, M., Alexander, C. R., Smirnova, T. G., et al. (2016). A North American hourly assimilation and model forecast cycle: The rapid refresh. *Monthly Weather Review*, *144*(4), 1669–1694. https://doi.org/10.1175/Mwr-D-15-0242.1

Bonin, T. A., Choukulkar, A., Brewer, W. A., Sandberg, S. P., Weickmann, A. M., Pichugina, Y. L., et al. (2017). Evaluation of turbulence measurement techniques from a single Doppler lidar. *Atmospheric Measurement Techniques*, *10*(8), 3021–3039. https://doi.org/10.5194/amt-10-3021-2017

Borbon, A., Gilman, J. B., Kuster, W. C., Grand, N., Chevaillier, S., Colomb, A., et al. (2013). Emission ratios of anthropogenic volatile organic compounds in northern mid-latitude megacities: Observations versus emission inventories in Los Angeles and Paris. *Journal of Geophysical Research: Atmospheres*, *118*(4), 2041–2057. https://doi.org/10.1002/jgrd.50059

Boulder, A. I. R. (2025). Bringing air quality monitoring to the Colorado front range [Dataset]. Retrieved from https://www.bouldair.com

Broderick, B. M., & Marnane, I. S. (2002). A comparison of the C_2–C_9 hydrocarbon compositions of vehicle fuels and urban air in Dublin, Ireland. *Atmospheric Environment*, *36*(6), 975–986. https://doi.org/10.1016/S1352-2310(01)00472-1

Brown, S. S., Thornton, J. A., Keene, W. C., Pszenny, A. A. P., Sive, B. C., Dubé, W. P., et al. (2013). Nitrogen, aerosol composition and halogens on a tall tower (NACHTT): Overview of a wintertime air chemistry field study in the front range urban corridor of Colorado. *Journal of Geophysical Research: Atmospheres*, *118*, 8067–8085. https://doi.org/10.1002/jgrd.50537

Caputi, D., Helmig, D., Darby, L. S., Greenberg, G., Hueber, J., Simoncic, S., & Ortega, J. (2025). Late winter Ozone and PM 2.5 NAAQS exceedance in the Northern Colorado front range in relation to oil and natural gas emissions. *Journal of Geophysical Research: Atmospheres*, *130*(9). https://doi.org/10.1029/2024jd041862

Carter, W. P. L., & Seinfeld, J. H. (2012). Winter ozone formation and VOC incremental reactivities in the upper Green River basin of Wyoming. *Atmospheric Environment*, *50*, 255–266. https://doi.org/10.1016/j.atmosenv.2011.12.025

Cheadle, L. C., Oltmans, S. J., Petron, G., Schnell, R. C., Mattson, E. J., Herndon, S. C., et al. (2017). Surface ozone in the Colorado northern front range and the influence of oil and gas development during FRAPPE/DISCOVER-AQ in summer 2014. *Elementa-Sci Anthrop*, *5*, ARTN 61. https://doi.org/10.1525/elementa.254

Choukulkar, A., Brewer, W. A., Sandberg, S. P., Weickmann, A., Bonin, T. A., Hardesty, R. M., et al. (2017). Evaluation of single and multiple Doppler lidar techniques to measure complex flow during the XPIA field campaign. *Atmospheric Measurement Techniques*, *10*(1), 247–264. https://doi.org/10.5194/amt-10-247-2017

de Gouw, J. A., Gilman, J. B., Borbon, A., Warneke, C., Kuster, W. C., Goldan, P. D., et al. (2012). Increasing atmospheric burden of ethanol in the United States. *Geophysical Research Letters*, *39*(15), Artn L15803. https://doi.org/10.1029/2012gl052109

Dix, B., Li, M., Roosenbrand, E., Francoeur, C., Brown, S. S., Gilman, J. B., et al. (2023). Sources of formaldehyde in US oil and gas production regions. *ACS Earth and Space Chemistry*, *7*(12), 2444–2457. https://doi.org/10.1021/acsearthspacechem.3c00203

Edwards, P. M., Brown, S. S., Roberts, J. M., Ahmadov, R., Banta, R. M., deGouw, J. A., et al. (2014). High winter ozone pollution from carbonyl photolysis in an oil and gas basin. *Nature*, *514*(7522), 351–354. https://doi.org/10.1038/nature13767

Edwards, P. M., Young, C. J., Aikin, K., deGouw, J., Dubé, W. P., Geiger, F., et al. (2013). Ozone photochemistry in an oil and natural gas extraction region during winter: Simulations of a snow-free season in the Uintah Basin, Utah. *Atmospheric Chemistry and Physics*, *13*(17), 8955–8971. https://doi.org/10.5194/acp-13-8955-2013

Flocke, F., Pfister, G., Crawford, J. H., Pickering, K. E., Pierce, G., Bon, D., & Reddy, P. (2020). Air quality in the northern Colorado front range metro area: The front range air pollution and photochemistry experiment (FRAPPE). *J. Geophys. Res.-Atmos.*, *125*(2), e2019JD031197. https://doi.org/10.1029/2019JD031197.)

Gelaro, R., McCarty, W., Suárez, M. J., Todling, R., Molod, A., Takacs, L., et al. (2017). The Modern-Era Retrospective Analysis for Research and Applications, Version 2 (MERRA-2). *Journal of Climate*, *30*(14), 5419–5454. https://doi.org/10.1175/Jcli-D-16-0758.1

Gentner, D. R., Harley, R. A., Miller, A. M., & Goldstein, A. H. (2009). Diurnal and seasonal variability of gasoline-related volatile organic compound emissions in Riverside, California. *Environmental Science & Technology*, *43*(12), 4247–4252. https://doi.org/10.1021/es9006228

Gentner, D. R., Worton, D. R., Isaacman, G., Davis, L. C., Dallmann, T. R., Wood, E. C., et al. (2013). Chemical composition of gas-phase organic carbon emissions from motor vehicles and implications for ozone production. *Environmental Science & Technology*, *47*(20), 11837–11848. https://doi.org/10.1021/es401470e

Gilman, J. B., Lerner, B. M., Kuster, W. C., & de Gouw, J. A. (2013). Source signature of volatile organic compounds from oil and natural gas operations in northeastern Colorado. *Environmental Science & Technology*, *47*(3), 1297–1305. https://doi.org/10.1021/es304119a

Global Modeling and Assimilation Office (GMAO). (2015). MERRA-2 inst3_3d_asm_Np: 3d,3-Hourly,Instantaneous,Pressure-Level,Assimilation,Assimilated meteorological fields V5.12.4, Greenbelt, MD, USA, Goddard Earth Sciences data and information services center (GES DISC). https://doi.org/10.5067/QBZ6MG944HW0. Accessed: [February 19, 2025].

Green, J. R., Fiddler, M. N., Fibiger, D. L., McDuffie, E. E., Aquino, J., Campos, T., et al. (2021). Wintertime formaldehyde: Airborne observations and source apportionment over the eastern United States. *Journal of Geophysical Research: Atmospheres*, *126*(5), ARTN e2020JD033518. https://doi.org/10.1029/2020JD033518

Harkins, C., McDonald, B. C., Henze, D. K., & Wiedinmyer, C. (2021). A fuel-based method for updating mobile source emissions during the COVID-19 pandemic. *Environmental Research Letters*, *16*(6), 065018. https://doi.org/10.1088/1748-9326/ac0660

He, J., Harkins, C., O'Dell, K., Li, M., Francoeur, C., Aikin, K. C., et al. (2023). COVID-19 perturbation on US air quality and human health impact assessment. *PNAS Nexus*, *3*(1). ARTN pgad483. https://doi.org/10.1093/pnasnexus/pgad483

Helmig, D. (2020). Air quality impacts from oil and natural gas development in Colorado. *Elementa-Sci Anthrop*, *8*. ARTN 4. https://doi.org/10.1525/elementa.398

Helmig, D., Ganzeveld, L., Butler, T., & Oltmans, S. J. (2007). The role of ozone atmosphere-snow gas exchange on polar, boundary-layer tropospheric ozone - A review and sensitivity analysis. *Atmospheric Chemistry and Physics*, *7*(1), 15–30. https://doi.org/10.5194/acp-7-15-2007

Helmig, D., Thompson, C. R., Evans, J., Boylan, P., Hueber, J., & Park, J. H. (2014). Highly elevated atmospheric levels of volatile organic compounds in the Uintah Basin, Utah. *Environmental Science & Technology*, *48*(9), 4707–4715. https://doi.org/10.1021/es405046r

Jaffe, D. A., Cooper, O. R., Fiore, A. M., Henderson, B. H., Tonneson, G. S., Russell, A. G., et al. (2018). Scientific assessment of background ozone over the U.S.: Implications for air quality management. *Elem Sci Anth*, *6*(1), 56. https://doi.org/10.1525/elementa.309

Karstadt, M., Callaghan, B., United States. Environmental Protection Agency, & Office of Air and Radiation (1993). *The plain English guide to the Clean Air Act*. U.S. Environmental Protection Agency For sale by the U.S. G.P.O., Supt. of Docs., 28.

Keller, C. A., Knowland, K. E., Duncan, B. N., Liu, J., Anderson, D. C., Das, S., et al. (2021). Description of the NASA GEOS composition forecast modeling system GEOS-CF v1.0. *Journal of Advances in Modeling Earth Systems*, *13*(4), e2020MS002413. https://doi.org/10.1029/2020MS002413

Knowland, K. E., Keller, C. A., Wales, P. A., Wargan, K., Coy, L., Johnson, M. S., et al. (2022). NASA GEOS composition forecast modeling system GEOS-CF v1.0: Stratospheric composition. *Journal of Advances in Modeling Earth Systems*, *14*(6), e2021MS002852. https://doi.org/10.1029/2021MS002852

Knowland, K. E., Ott, L. E., Duncan, B. N., & Wargan, K. (2017). Stratospheric intrusion-influenced ozone air quality exceedances investigated in the NASA MERRA-2 reanalysis. *Geophysical Research Letters*, *44*(20), 10691–10701. https://doi.org/10.1002/2017GL074532

Kumar, R., Bhardwaj, P., Pfister, G., Drews, C., Honomichl, S., & D'Attilo, G. (2021). Description and evaluation of the fine particulate matter forecasts in the NCAR regional air quality forecasting system. *Atmosphere*, *12*(3), 302. ARTN 302. https://doi.org/10.3390/atmos12030302

Langford, A. O., Aikin, K. C., Eubank, C. S., & Williams, E. J. (2009). Stratospheric contribution to high surface ozone in Colorado during springtime. *Geophysical Research Letters*, *36*(12). https://doi.org/10.1029/2009GL038367

Langford, A. O., Alvarez II, R. J., Kirgis, G., Senff, C. J., Caputi, D., Conley, S. A., et al. (2019). Intercomparison of lidar, aircraft, and surface ozone measurements in the San Joaquin valley during the California Baseline Ozone Transport Study (CABOTS). *Atmospheric Measurement Techniques*, *12*(3), 1889–1904. https://doi.org/10.5194/amt-12-1889-2019

Langford, A. O., Senff, C. J., Alvarez II, R. J., Aikin, K. C., Baidar, S., Bonin, T. A., et al. (2022). The Fires, Asian, and Stratospheric Transport–Las Vegas Ozone Study (FAST-LVOS). *Atmospheric Chemistry and Physics*, *22*(3), 1707–1737. https://doi.org/10.5194/acp-22-1707-2022

Lareau, N. P., Crosman, E., Whiteman, C. D., Horel, J. D., Hoch, S. W., Brown, W. O. J., & Horst, T. W. (2013). The persistent cold-air pool study. *Bulletin of the American Meteorological Society*, *94*(1), 51–63. https://doi.org/10.1175/Bams-D-11-00255.1

LT Environmental. (2007). Greater Wattenberg Area Baseline Study Report. *Colorado Oil and Gas Conservation Commission (COGCC)*.

Lyman, S., & Tran, T. (2015). Inversion structure and winter ozone distribution in the Uintah Basin, Utah, USA. *Atmospheric Environment*, *123*, 156–165. https://doi.org/10.1016/j.atmosenv.2015.10.067

Mansfield, M. L., & Hall, C. F. (2018). A survey of valleys and basins of the Western United States for the capacity to produce winter ozone. *Journal of the Air & Waste Management Association*, *68*(9), 909–919. https://doi.org/10.1080/10962247.2018.1454356

Martin, R., Moore, K., Mansfield, M. L., Hill, S., Harper, K., & Shorthill, H. (2011). Final report: Uinta Basin Winter Ozone and Air Quality Study.

McCaffrey, K., Wilczak, J. M., Bianco, L., Grimit, E., Sharp, J., Banta, R., et al. (2019). Identification and characterization of persistent cold pool events from temperature and wind profilers in the Columbia River Basin. *Journal of Applied Meteorology and Climatology*, *58*(12), 2533–2551. https://doi.org/10.1175/Jamc-D-19-0046.1

McDuffie, E. E., Edwards, P. M., Gilman, J. B., Lerner, B. M., Dubé, W. P., Trainer, M., et al. (2016). Influence of oil and gas emissions on summertime ozone in the Colorado northern front range. *J. Geophys. Res.-Atmos.*, *121*(14), 8712–8729. https://doi.org/10.1002/2016jd025265

NASA/GSFC. (2025). Aeronet [Dataset]. Retrieved from https://aeronet.gsfc.nasa.gov

NCAR/ACOM. (2025). WRF-CHEM forecast maps [Dataset]. Retrieved from https://www.acom.ucar.edu/firex-aq/forecast.shtml

Neemann, E. M., Crosman, E. T., Horel, J. D., & Avey, L. (2015). Simulations of a cold-air pool associated with elevated wintertime ozone in the Uintah Basin, Utah. *Atmospheric Chemistry and Physics*, *15*(1), 135–151. https://doi.org/10.5194/acp-15-135-2015

Nelson, P. F., & Quigley, S. M. (1984). The hydrocarbon composition of exhaust emitted from gasoline fueled vehicles. *Atmospheric Environment*, *18*(1), 79–87. https://doi.org/10.1016/0004-6981(84)90230-0

Newchurch, M. J., Kuang, S., Leblanc, T., Alvarez II, R. J., Langford, A. O., Senff, C. J., et al. (2016). TOLNet - A tropospheric ozone lidar profiling network for satellite continuity and process studies. *EPJ Web of Conferences*, *119*, 20001. https://doi.org/10.1051/epjconf/201611920001

NOAA Chemical Sciences Laboratory. (2025). COVID air quality study (COVID-AQS) 2020 [Dataset]. *NOAA Chemical Sciences Laboratory*. Retrieved from https://csl.noaa.gov/groups/csl7/measurements/2020covid-aqs/

Oltmans, S., Schnell, R., Johnson, B., Pétron, G., Mefford, T., & Neely, R., III. (2014). Anatomy of wintertime ozone associated with oil and natural gas extraction activity in Wyoming and Utah. *Elementa: Science of the Anthropocene*, *2*. https://doi.org/10.12952/journal.elementa.000024

Peischl, J., Aikin, K. C., McDonald, B. C., Harkins, C., Middlebrook, A. M., Langford, A. O., et al. (2023). Quantifying anomalies of air pollutants in 9 US cities during 2020 due to COVID-19 lockdowns and wildfires based on decadal trends. *Elementa-Sci Anthrop*, *11*(1). ARTN 00029. https://doi.org/10.1525/elementa.2023.00029

Pétron, G., Frost, G., Miller, B. R., Hirsch, A. I., Montzka, S. A., Karion, A., et al. (2012). Hydrocarbon emissions characterization in the Colorado front range: A pilot study. *Journal of Geophysical Research*, *117*(D4). https://doi.org/10.1029/2011jd016360

Pétron, G., Karion, A., Sweeney, C., Miller, B. R., Montzka, S. A., Frost, G. J., et al. (2014). A new look at methane and nonmethane hydrocarbon emissions from oil and natural gas operations in the Colorado Denver-Julesburg basin. *J. Geophys. Res.-Atmos.*, *119*(11), 6836–6852. https://doi.org/10.1002/2013jd021272

Pollack, I. B., Helmig, D., O'Dell, K., & Fischer, E. V. (2021). Seasonality and source apportionment of nonmethane volatile organic compounds at Boulder Reservoir, Colorado, between 2017 and 2019. *J. Geophys. Res.-Atmos.*, *126*(9), e2020JD034234. https://doi.org/10.1029/2020JD034234

Rappenglück, B., Ackermann, L., Alvarez, S., Golovko, J., Buhr, M., Field, R. A., et al. (2014). Strong wintertime ozone events in the Upper Green River Basin, Wyoming. *Atmospheric Chemistry and Physics*, *14*(10), 4909–4934. https://doi.org/10.5194/acp-14-4909-2014

Rickly, P. S., Coggon, M. M., Aikin, K. C., Alvarez, R. J., II, Baidar, S., Gilman, J. B., et al. (2023). Influence of wildfire on urban ozone: An observationally constrained box modeling study at a site in the Colorado front range. *Environmental Science & Technology*, *57*(3), 1257–1267. https://doi.org/10.1021/acs.est.2c06157

Rossabi, S., & Helmig, D. (2018). Changes in atmospheric butanes and pentanes and their isomeric ratios in the Continental United States. *J. Geophys. Res.-Atmos.*, *123*(7), 3772–3790. https://doi.org/10.1002/2017jd027709

Schnell, R. C., Johnson, B. J., Oltmans, S. J., Cullis, P., Sterling, C., Hall, E., et al. (2016). Quantifying wintertime boundary layer ozone production from frequent profile measurements in the Uinta Basin, UT, oil and gas region. *J. Geophys. Res.-Atmos.*, *121*(18), 11038–11054. https://doi.org/10.1002/2016jd025130

Schnell, R. C., Oltmans, S. J., Neely, R. R., Endres, M. S., Molenar, J. V., & White, A. B. (2009). Rapid photochemical production of ozone at high concentrations in a rural site during winter. *Nature Geoscience*, *2*(2), 120–122. https://doi.org/10.1038/Ngeo415

Sillman, S., & Samson, P. J. (1995). Impact of temperature on oxidant photochemistry in urban, polluted rural and remote environments. *Journal of Geophysical Research*, *100*(D6), 12–11508. https://doi.org/10.1029/94jd02146

Stein, A. F., Draxler, R. R., Rolph, G. D., Stunder, B. J. B., Cohen, M. D., & Ngan, F. (2015). NOAA'S HYSPLIT atmospheric transport and dispersion modeling system. *Bulletin of the American Meteorological Society*, *96*(12), 2059–2077. https://doi.org/10.1175/Bams-D-14-00110.1

Swarthout, R. F., Russo, R. S., Zhou, Y., Hart, A. H., & Sive, B. C. (2013). Volatile organic compound distributions during the NACHTT campaign at the Boulder Atmospheric Observatory: Influence of urban and natural gas sources. *J. Geophys. Res.-Atmos.*, *118*(18), 10614–10637. https://doi.org/10.1002/jgrd.50722

Thompson, C. R., Hueber, J., & Helmig, D. (2015). Influence of oil and gas emissions on ambient atmospheric non-methane hydrocarbons in residential areas of northeastern Colorado. *Elem Sci Anth*, *3*. https://doi.org/10.12952/journal.elementa.000035

TOLNet science team. (2025). Tropospheric ozone lidar network database [Dataset]. *NASA Langley Research Center*. https://doi.org/10.5067/LIDAR/OZONE/TOLNET

U.S. (1976). *U.S. standard atmosphere, 1976 rep. NOAA-S/T 76-1562*. NOAA.

US Environmental Protection Agency. (2025). Air quality system data mart. [internet database] available via Retrieved from https://www.epa.gov/outdoor-air-quality-data

Wolfe, G. M., Marvin, M. R., Roberts, S. J., Travis, K. R., & Liao, J. (2016). The framework for 0-D atmospheric modeling (F0AM) v3.1. *Geoscientific Model Development*, *9*(9), 3309–3319. https://doi.org/10.5194/gmd-9-3309-2016

References From the Supporting Information

Johnson, B. J., Oltmans, S. J., Vomel, H., Smit, H. G. J., Deshler, T., & Kroger, C. (2002). Electrochemical concentration cell (ECC) ozonesonde pump efficiency measurements and tests on the sensitivity to ozone of buffered and unbuffered ECC sensor cathode solutions. *Journal of Geophysical Research*, *107*(D19), ACH8-1–ACH8-18. https://doi.org/10.1029/2001jd000557

Kupc, A., Williamson, C., Wagner, N. L., Richardson, M., & Brock, C. A. (2018). Modification, calibration, and performance of the ultra-high sensitivity aerosol spectrometer for particle size distribution and volatility measurements during the atmospheric tomography mission (ATom) airborne campaign. *Atmospheric Measurement Techniques*, *11*(1), 369–383. https://doi.org/10.5194/amt-11-369-2018

Lerner, B. M., Gilman, J. B., Aikin, K. C., Atlas, E. L., Goldan, P. D., Graus, M., et al. (2017). An improved, automated whole air sampler and gas chromatography mass spectrometry analysis system for volatile organic compounds in the atmosphere. *Atmospheric Measurement Techniques*, *10*(1), 291–313. https://doi.org/10.5194/amt-10-291-2017

He, J., Lamplugh, A., Langford, A. O., McDonald, B. C., Peischl, J., Robinson, M. A., et al. (2023). Influence of wildfire on urban ozone: An observationally constrained box modeling study at a site in the Colorado front range. *Environmental Science & Technology*, *57*(3), 1257–1267. https://doi.org/10.1021/acs.est.2c06157

Yuan, B., Koss, A., Warneke, C., Gilman, J. B., Lerner, B. M., Stark, H., & de Gouw, J. A. (2016). A high-resolution time-of-flight chemical ionization mass spectrometer utilizing hydronium ions (H3O+ ToF-CIMS) for measurements of volatile organic compounds in the atmosphere. *Atmospheric Measurement Techniques*, *9*(6), 2735–2752. https://doi.org/10.5194/amt-9-2735-2016